Engineering Structures 281 (2023) 115758

Contents lists available at ScienceDirect

Engineering Structures

journal homepage: www.elsevier.com/locate/engstruct

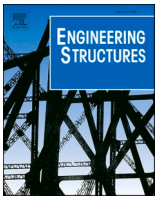

# Inelastic cyclic response of RBS connections with jumbo sections

D.V. Bompa [a,b,*], A.Y. Elghazouli [b], T. Bogdan [c], M.R. Eatherthon [d], R.T. Leon [d]

[a] School of Sustainability, Civil and Environmental Engineering, University of Surrey, GU2 7HX, UK
[b] Department of Civil and Environmental Engineering, Imperial College London, SW7 2AZ, UK
[c] ArcelorMittal Global Research and Development Esch, Esch sur Alzette, Luxembourg
[d] Department of Civil and Environmental Engineering, Virginia Tech, Blacksburg, VA 20461, USA

ARTICLE INFO

*Keywords:*
Reduced beam sections
Welded steel connections
Seismic design
Cyclic response
Non-linear analysis

ABSTRACT

This paper examines the cyclic performance of reduced beam section (RBS) moment connections incorporating larger member sizes than those allowed in the current seismic provisions for prequalified steel connections, through experimentally validated three-dimensional nonlinear numerical assessments. Validations of the adopted nonlinear finite element procedures are carried out against experimental results from two test series, including four full-scale RBS connections comprising large structural members, outside the prequalification limits. After gaining confidence in the ability of the numerical models to predict closely the full inelastic response and failure modes, parametric investigations are undertaken. Particular attention is given to assessing the influence of the RBS-to-column capacity ratio as well as the RBS geometry and location on the overall response. The numerical results and test observations provide a detailed insight into the structural behavior, including strength, ductility, and failure modes of large RBS connections. It is shown that connections which consider sections beyond the code limits, by up to two times the weight or beam depth limits, developed a stable inelastic response characterized by beam flexural yielding and inelastic local buckling. However, connections with very large beam sections, up to three-times the typically prescribed limits, exhibited significant hardening resulting in severe demands at the welds, hence increasing susceptibility to weld fracture and propagation through the column. The findings from this study point to the need, in jumbo sections with thick flanges, for a deeper RBS cut than currently specified in design, to about 66% of the total beam width. This modification would be required to promote a response governed by extensive yielding at the RBS while reducing the excessive strain demands at the beam-to-column welds. Moreover, for connections incorporating relatively deep columns, it is shown that more stringent design requirements need to be followed, combined with appropriate bracing outside the RBS, to avoid out-of-plane rotation.

## 1. Introduction

Steel moment frames are typically designed with rigid full-strength connections using welded or combined welded/bolted configurations. Such connections are designed with sufficient overstrength such that dissipative zones develop primarily in the beams [1] with or without dissipative contributions from the panel zones [2]. Assessments of damage in past seismic events attributed steel beam-to-column connection fractures to several factors including excessive strain demands and complex triaxial stress states as well as inadequate weld qualities and procedures [3,4]. These assessments included various research investigations to develop new design and detailing approaches as well as retrofitting techniques. In addition to the use of haunches, continuity plates or other stiffening components, another strategy consists of weakening the beam by producing a Reduced Beam Section (RBS). This RBS can be provided through polygonal, trapezoidal, straight, or radius cuts, with each arrangement leading to different cyclic performance [5–7].

Previous studies showed that RBS connections with polygonal cuts at the reduced section typically develop a good hysteretic response, whilst straight cuts may lead to poor performance of the connection caused by stress concentrations at the corners of the cut [3,8]. Although trapezoidal cuts promote a uniformly distributed yielding pattern, it was shown that fractures can initiate at the corners at the returns of the

* Corresponding author at: School of Sustainability, Civil and Environmental Engineering, University of Surrey, GU2 7HX, UK.
*E-mail addresses:* d.bompa@surrey.ac.uk (D.V. Bompa), a.elghazouli@imperial.ac.uk (A.Y. Elghazouli), teodora.bogdan@arcelormittal.com (T. Bogdan), meather@vt.edu (M.R. Eatherthon), rleon@vt.edu (R.T. Leon).

https://doi.org/10.1016/j.engstruct.2023.115758
Received 22 August 2022; Received in revised form 9 January 2023; Accepted 2 February 2023
Available online 17 February 2023

tapered section [9,10]. Other studies showed that straight RBS cuts with rounded corners may fail at the welds after a limited number of inelastic cycles due to high stress concentration and localized plastic strains in the welds [11]. In contrast, the radius cut RBS, later adopted in North American standards, was shown to exhibit a more ductile behavior [12]. Moreover, if proportioned properly, radius cut RBS connections offer a significant reduction in the inelastic strain demand at the beam flange weld, minimizing the risk of fracture compared to other RBS geometries [7].

Recent experimental studies indicated that both monotonic and cyclic loading protocols typically produce fractures at the bottom flange of the reduced section that may propagate along the web [13]. However, rotational capacities under monotonic loading were shown to be about two fold larger than those under cyclic loading. Moreover, conventional non-RBS connections could experience premature fractures at the beam flange to column welds, whilst those with RBS typically develop more stable hysteretic behavior and enhanced energy dissipation capacity, with plasticity developing mainly at the reduced section [9,14]. Although the radius cut RBS enhanced cyclic performance compared to other types, the geometry of the cut had a significant influence in terms of plastic distribution and, ultimately, failure mode. A smaller cut than stipulated in the current design codes could lead to severe yielding and fracture in the vicinity of the column face outside of the RBS region [15,16]. According to the North American design procedures (ANSI/AISC 358–16 [17]), the limits on the RBS geometry are a function of the beam width ($b_f$) and depth ($d$) as follows: the distance from the column face to the start of the cut, a, varies within $0.5 \times b_f \leq a \leq 0.75 \times b_f$; the length of the RBS cut, $b$, must be in the range $0.65 \times d \leq b \leq 0.85 \times d$, and the depth of cut at the middle of the RBS, $c$, must be between $0.1 \times b_f \leq c \leq 0.25 \times b_f$. The main connection dimensions are shown in Fig. 1a, b. These ranges are similar in Eurocode 8–3 [18]: $a = 0.5 \times b_f$, $b = 0.75 \times d$ and $c = 0.20 \times b_f$.

It is generally accepted that favorable failure modes of RBS connections are characterized by extensive yielding at the RBS, followed by or coinciding with limited yielding of the PZ and ultimately local flange buckling at the RBS [19,20]. The latter also controls the connection peak load / softening behavior and limits the level of hardening. The reduction of beam flanges may also result in early local buckling in the beam web compared to conventional beams [20]. Such effects are typically minimized or eliminated in the presence of a composite floor slab [21–23]. The presence of slabs can also greatly reduce the out of plane column rotation and warping observed in RBS connections [24]. This may be particularly significant for deep columns, often preferred in design as an economic solution to control seismic drifts in moment frames [25,26].

The findings from previous studies were largely based on RBS tests with beam sizes up to W36 × 302 (W920 × 420 × 449) 302 lb/ft (449 kg/m) and column sizes up to W14 × 550 (W360 × 410 × 818) 550 lbs/ft (818 kg/m) [3], which led to the limits in current North American prequalification standards [17]. In order to examine the suitability of extending the RBS related provisions of ANSI/AISC 358–16 [17] to larger sections with nominal depths up to 1100 mm (W44 × 408 or W1100 × 400 × 607) and weights up to 925 lb/ft (1377 kg/m) corresponding to W36 × 925 (W920 × 420 × 1377), an experimental investigation was undertaken as part of a collaborative research project [27]. In this paper, nonlinear parametric investigations on complementary models with sections outside the test database were constructed and analyzed to evaluate the suitability of extending current prequalification limits. These simulations aim at evaluating the inelastic cyclic response of RBS connections with jumbo section designed to specifications but with sizes outside of the prequalification limits. This paper, which propose new practical recommendations for the design of such connections and specifies the suitability of various connection configurations for prequalification, is organised as described below.

The results from an experimental program on four RBS connections carried out within the above-mentioned project [28,29], as well as three RBS connections tests with deep columns [24,30] described in Section 2, are used for validation of the nonlinear finite element modelling procedures employed in this paper and covered in Section 3. The test and numerical stiffness, strength and ductility characteristics are examined in detail in Section 2 and 3 of this paper, respectively. Existing analytical procedures to estimate the fracture life and critical buckling strains are employed and validated against the tests and simulations to evaluate the governing response of the investigated connections in Section 4. Within the same section, the plastic strain distribution is examined for the main connection components of the seven RBS connections. After validating

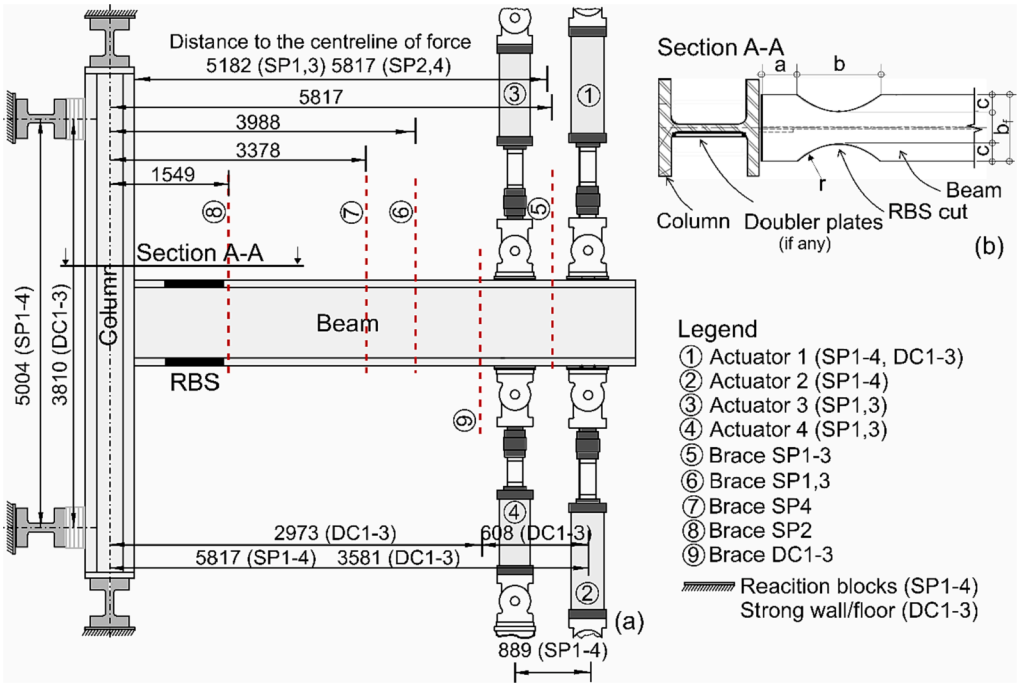


**Fig. 1.** (a) Schematic representation of the testing arrangement for examined specimens, b) Plan detail of the examined connections.

the nonlinear numerical and analytical procedures, a number of parametric studies are carried out in Section 5, in which RBS connections designed to specifications but with sizes outside of the prequalification limits, are subjected to cyclic loading. Based on the results, new practical recommendations are proposed and discussed in Section 5 for the use of RBS connections with jumbo beam and column members.

## 2. Experimental assessments

The first test series used for validation comprised four RBS connections (SP1-4) incorporating very large steel sections [28,29], whilst the second test series included three RBS specimens (DC1-3) with deep columns [24,30]. All specimens from the first set had at least one parameter outside the current prequalification limits, whilst the parameters of specimens from the second experimental dataset are within the prequalification limits. Tables 1 and 2 list the RBS parameters (see Fig. 1a,b) and material strengths of the seven specimens. In both series, the columns were restrained against translation at both ends and lateral cyclic displacements were applied at the end of a cantilever beam, as illustrated in Fig. 1a.

### 2.1. Specimens and testing arrangements

#### 2.1.1. SP1-4

Four external RBS beam-column assemblages, consisting of around 6.2 m long column and a 6.1 m long beam provided with a radius cut RBS determined in accordance with code procedures [17], were tested under cyclic loading [28,29]. As shown in Fig. 2a,b, the sizes of the connection components are larger in comparison to existing tests [25]. Specimens SP1 and SP3 had the same column section (Table 1). The beam section of SP1 was midway between the current prequalification limit 447 kg/m (302 lb/ft) and the largest available rolled section 1377 kg/m (925 lb/ft), whilst the beam section of SP3 was the heaviest W36 available. Specimens SP2 and SP4 had the lightest and heaviest available W44 beam sections. These were connected to W14 × 342 and W40 × 503 columns, respectively. The column sizes were chosen to have sufficient flexural and PZ strength to satisfy ANSI/AISC 341–16 [31] and ANSI/AISC 360–16 [32] requirements. SP3 was provided with a 31.8 mm (1.25 in.) doubler plate to increase the PZ strength beyond code requirements because preliminary finite element modeling suggested code panel zone requirements were insufficient [33].

The beams of SP1, SP2 and SP4 were fabricated from A992 Grade 50 steel [34], the beams of SP3 and columns of SP1-4 from A913 Grade 65 steel [35], and doubler plates from A572 Grade 50 steel [36]. The measured yield and ultimate strengths presented in Table 2, were obtained from full-thickness tensile coupon tests in accordance with ASTM A370 [37] by the manufacturer. All specimens were welded using a dual-shielded flux-cored arc weld (FCAW) process with E71T-1 or E71T-8 wire. The Charpy V-notch (CVN) toughness of this electrode reported by the manufacturer is 42 J at −29 °C and 75 J at −29 °C, respectively, which is above the minimum specified values according to ANSI/AISC 358–16 [17].

The specimens were tested in a reaction frame attached to the laboratory strong floor by means of steel stub elements. A cyclic displacement was applied at the beam end in accordance with the special moment frame (SMF) qualification protocol described in ANSI/AISC 341–16 [31]. The testing equipment included four MTS actuators, two at each side of the beam component [29] and the specimens were laterally braced at locations shown in Fig. 1a. According to AISC 341–16 SMF qualification criteria, a beam-column connection is deemed successful if the tested specimen completes one cycle at 4 % story drift while retaining 80 % of the nominal plastic moment strength of the unreduced beam section.

#### 2.1.2. DC1-3

Specimens DC1-3, shown in Fig. 1, also represent external beam-column assemblies designed for SMF [24,30]. The design of the connections was based on the AISC Seismic Provisions [38] and modified using specific procedures for RBS regions [39]. Specimens DC1 and DC2 had the same beam size W36 × 150 and different columns: W27 × 146 and W27 × 194, respectively. Specimen DC3 had the same beam and column geometry W27 × 194, with some differences in material properties (Tables 1 and 2).

The specified steel was A992 Grade 50 [34]. Material properties were assessed from tensile test coupons obtained from both web and flanges [24]. The specimens were welded with the column in an upright position with self-shielded flux-cored arc welding. The filler materials were E70T-6 for beam flange groove welds, and E71T-8 for connecting the remaining parts. These were specified to have a minimum Charpy V-Notch impact value of 27 J at −29 °C.

The specimens were tested in an upright position, and the column reacted against four stubs which were connected to a reaction wall [24].

**Table 1**
Specimen details.

| Spec. | Beam section | Column section | Continuity plates mm (in) | Doubler plates mm (in) | RBS cut a mm (in) | b mm (in) | c mm (in) |
|---|---|---|---|---|---|---|---|
| SP1 | W36 × 652 (W920 × 420 × 970) | W14 × 873 (W360 × 410 × 1299) | None | None | 335 (13.2) | 887 (34.9) | 80.5 (3.17) |
| SP2 | W44 × 230 (W1100 × 400 × 343) | W14 × 342 (W360 × 410 × 509) | None | None | 201 (7.9) | 709 (27.9) | 68.3 (2.7) |
| SP3 | W36 × 925 (W920 × 420 × 1377) | W14 × 873 (W360 × 410 × 1299) | None | 31.8 (1.25) | 236 (9.3) | 710 (27.9) | 99.3 (3.9) |
| SP4 | W44 × 408 (W1100 × 400 × 607) | W40 × 503 (W1000 × 400 × 748) | None | None | 304 (12.0) | 950 (37.4) | 85.3 (3.4) |
| DC1 | W36 × 150 (W920 × 310 × 223) | W27 × 146 (W690 × 360 × 217) | 25.4 (1.0) | 9.5 (0.4) | 228.6 (9.0) | 762.0 (30.0) | 76.2 (3.0) |
| DC2 | W36 × 150 (W920 × 310 × 223) | W27 × 194 (W690 × 360 × 289) | 25.4 (1.0) | None | 228.6 (9.0) | 762.0 (30.0) | 76.2 (3.0) |
| DC3 | W27 × 194 (W690 × 360 × 289) | W27 × 194 (W690 × 360 × 289) | 25.4 (1.0) | 15.9 (0.6) | 266.7 (10.5) | 609.6 (24.0) | 69.8 (2.8) |

Note: 1) the section types are first defined in the imperial system and then in the metric system (in brackets); 2) the last term in section type definition represents the weight of the profile; e.g for W 36 × 652 (W 920 × 420 × 970), the weight is 652 lb/ft (970 kg/m).

**Table 2**
Material properties.

| Specimen | Component | Section type | ASTM Grade | $f_{y,0.2\%}$ MPa (ksi) Flange | $f_u$ MPa (ksi) | $f_{y,0.2\%}$ MPa (ksi) Web | $f_u$ MPa (ksi) |
|---|---|---|---|---|---|---|---|
| SP1 | Beam | W 36 × 652 (W 920 × 420 × 970) | A992 | 416 (60.3) | 559 (81.1) | 416 (60.3) | 559 (81.1) |
| | Column | W 14 × 873 (W 360 × 410 × 1299) | A913 Gr. 65 | 448 (65) | 623 (90.4) | 448 (65) | 623 (90.4) |
| SP2 | Beam | W 44 × 230 (W 1100 × 400 × 343) | A992 | 461 (66.8) | 644 (93.4) | 461 (66.8) | 644 (93.4) |
| | Column | W 14 × 342 (W 360 × 410 × 509) | A913 Gr. 65 | 510 (73.9) | 642 (93.1) | 510 (73.9) | 642 (93.1) |
| SP3 | Beam | W 36 × 925 (W 920 × 420 × 1377) | A913 Gr. 65 | 470 (68.1) | 629 (91.3) | 470 (68.1) | 629 (91.3) |
| | Column | W 14 × 873 (W 360 × 410 × 1299) | A913 Gr. 65 | 448 (65) | 623 (90.4) | 448 (65) | 623 (90.4) |
| SP4 | Beam | W 44 × 408 (W 1100 × 400 × 607) | A992 | 447 (64.9) | 574 (83.2) | 447 (64.9) | 574 (83.2) |
| | Column | W 40 × 503 (W 1000 × 400 × 748) | A913 Gr. 65 | 504 (73.1) | 646 (93.7) | 504 (73.1) | 646 (93.7) |
| DC1 | Beam | W 36 × 150 (W 920 × 310 × 223) | A992 | 400 (58.0) | 455 (66.0) | 359 (52.0) | 445 (65.0) |
| | Column | W27 × 146 (W 690 × 360 × 217) | A992 | 358 (52.0) | 474 (69.0) | 344 (50.0) | 433 (63.0) |
| DC2 | Beam | W36 × 150 (W 920 × 310 × 223) | A992 | 400 (58.0) | 455 (66.0) | 359 (52.0) | 445 (65.0) |
| | Column | W27 × 194 (W 690 × 360 × 289) | A992 | 427 (62.0) | 453 (66.0) | 435 (63.0) | 449 (65.0) |
| DC3 | Beam | W27 × 194 (W 690 × 360 × 289) | A992 | 427 (62.0) | 453 (66.0) | 435 (63.0) | 449 (65.0) |
| | Column | W27 × 194 (W 690 × 360 × 289) | A992 | 375 (54.0) | 482 (70.0) | 383 (56.0) | 481 (70.0) |

Note: 1) the section types are first defined in the imperial system and then in the metric system (in brackets); 2) the last term in section type definition represents the weight of the profile; e.g for W 36 × 652 (W 920 × 420 × 970), the weight is 652 lb/ft (970 kg/m).

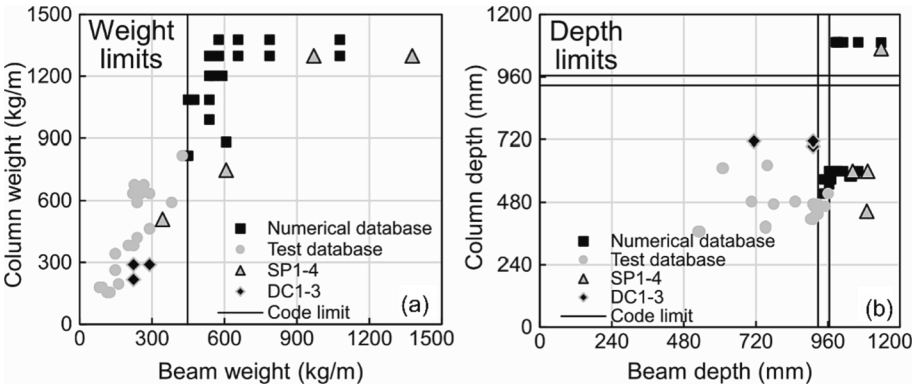


**Fig. 2.** Database details: a) Relationship between column and beam weight, b) Relationship between column and beam depth. Notes: Numerical database (Section 4 of this paper), Test database (Uang and Fan, 2001 [25]), SP1-4 (Landolfo et al., 2018 [28]; Paquette et al, 2021 [29]), DC1-3 (Chi and Uang, 2002 [24]), Code limit (ANSI/AISC 358–16 [17]).

**Table 3**
Test and numerical results.

| Specimen | Test $P_y$ (kN) | $P_u$ (kN) | $\theta_y$ (mrad) | $\theta_u$ (mrad) | Numerical $P_y$ (kN) | $P_u$ (kN) | $\theta_y$ (mrad) | $\theta_u$ (mrad) | Test/Numerical $P_y/P_y$ (-) | $P_u/P_u$ (-) | $\theta_y/\theta_y$ (-) | $\theta_u/\theta_u$ (-) |
|---|---|---|---|---|---|---|---|---|---|---|---|---|
| SP1 | 2439 | 3615 | 11.4 | 26.8 | 2682 | 3567 | 11.9 | 26.0 | 0.91 | 1.01 | 0.96 | 1.03 |
| SP2 | 855 | 1294 | 12.1 | 40.0 | 896 | 1290 | 13.3 | 41.2 | 0.95 | 1.00 | 0.91 | 0.97 |
| SP3 | 3647 | 5430 | 12.1 | 35.4 | 3806 | 5410 | 13.9 | 36.1 | 0.96 | 1.00 | 0.88 | 0.98 |
| SP4 | 1666 | 2289 | 8.1 | 24.4 | 1656 | 2362 | 9.9 | 24.3 | 1.01 | 0.97 | 0.82 | 1.00 |
| DC1 | 960 | 1103 | 37.6 | 54.7 | 919 | 1079 | 35.4 | 68.6 | 1.04 | 1.02 | 1.06 | 0.80 |
| DC2 | 953 | 1093 | 37.6 | 75.5 | 888 | 1030 | 34.5 | 70.5 | 1.07 | 1.06 | 1.09 | 1.07 |
| DC3 | 953 | 1250 | 37.6 | 144.7 | 999 | 1210 | 37.1 | 141.5 | 0.95 | 1.03 | 1.01 | 1.02 |
| | | | | | | | | AVG | 0.99 | 1.02 | 0.96 | 0.98 |
| | | | | | | | | COV | 0.06 | 0.03 | 0.10 | 0.09 |

The beam ends were restrained against twisting through a set of braces located at 2.97 m from the column center. The prescribed displacement was applied at the beam end using the standard SAC loading protocol [40], which was a precursor to the protocol from ANSI/AISC 341–16 [31].

### 2.2. Test results

#### 2.2.1. SP1-4

The test results are summarized in Table 3, while the overall force-chord rotation ($P$-$\theta$) curves are depicted in Fig. 3. Images of the test specimens in the plastic regime are shown in Fig. 4. The test force $P$ represents the sum of forces recorded by the actuators, whilst $\theta$ was calculated using test displacements recorded by string potentiometers located near the beam end, after adjusting for the rigid body motion. The yield force ($P_y$) and yield rotation ($\theta_y$), given in Table 3, represent deviation from linearity of the respective $P$-$\theta$ curves corresponding to first yield in the tested member [45], whilst $P_u$ and $\theta_u$ are the load and rotation corresponding to peak capacity. It should be noted that the chord rotation $\theta$, includes all sources of deformations in an RBS connection, namely: at the reduced section, panel zone, and the column.

Specimen SP1 reached flexural yielding, exhibited hardening, and ultimately failed, due to weld fracture at the bottom flange of the beam [29]. The load-rotation ($P$-$\theta$) curve is shown in Fig. 3a, and a close-up view of the connection at failure is depicted in Fig. 4a. The crack propagated across the column flange following an oblique pattern in the

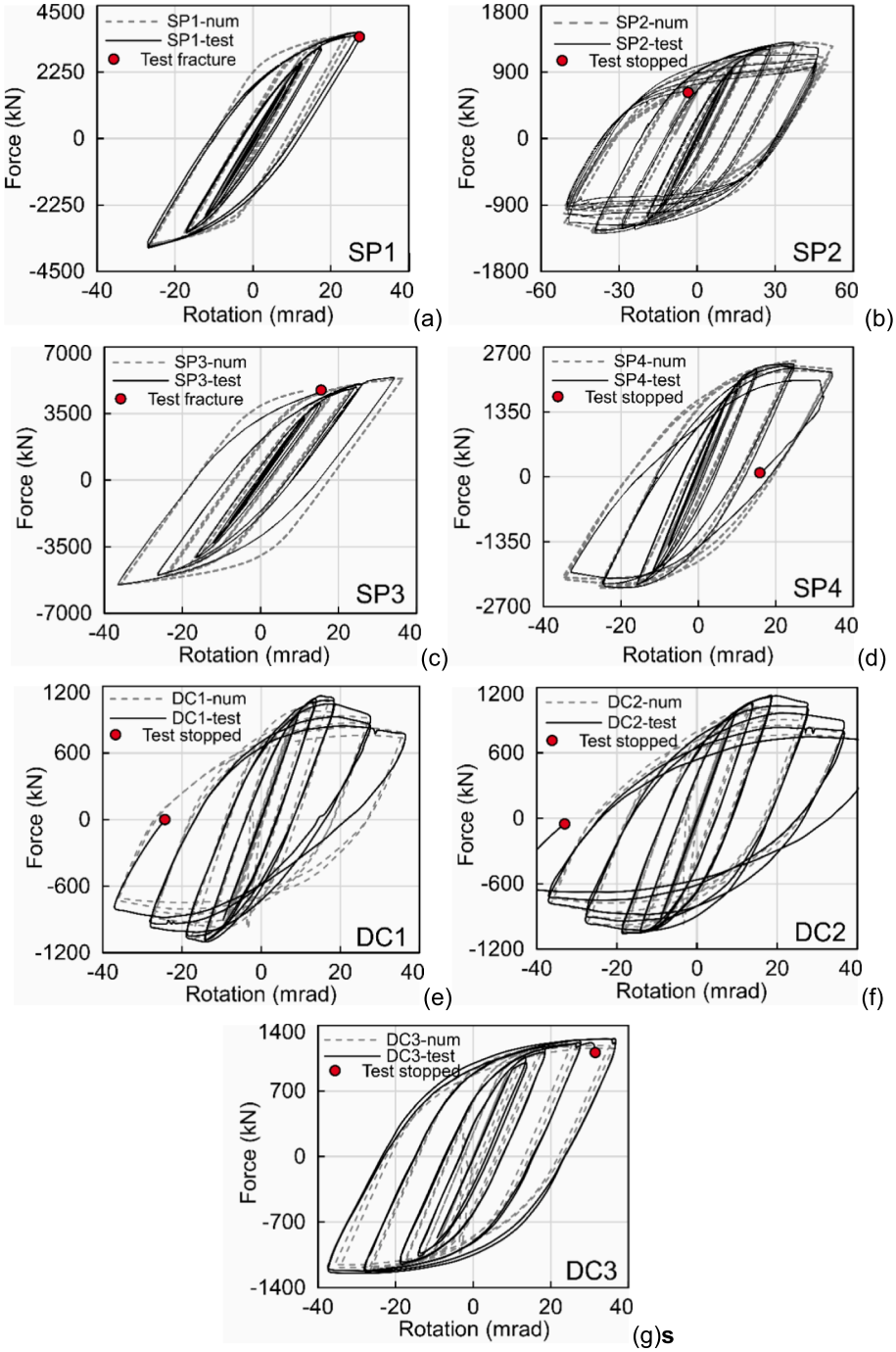


**Fig. 3.** Experimental and numerical force – rotation P-θ curves for: a) SP1, b) SP2, c) SP3, d) SP4, e) DC1, f) DC2, g) DC3.

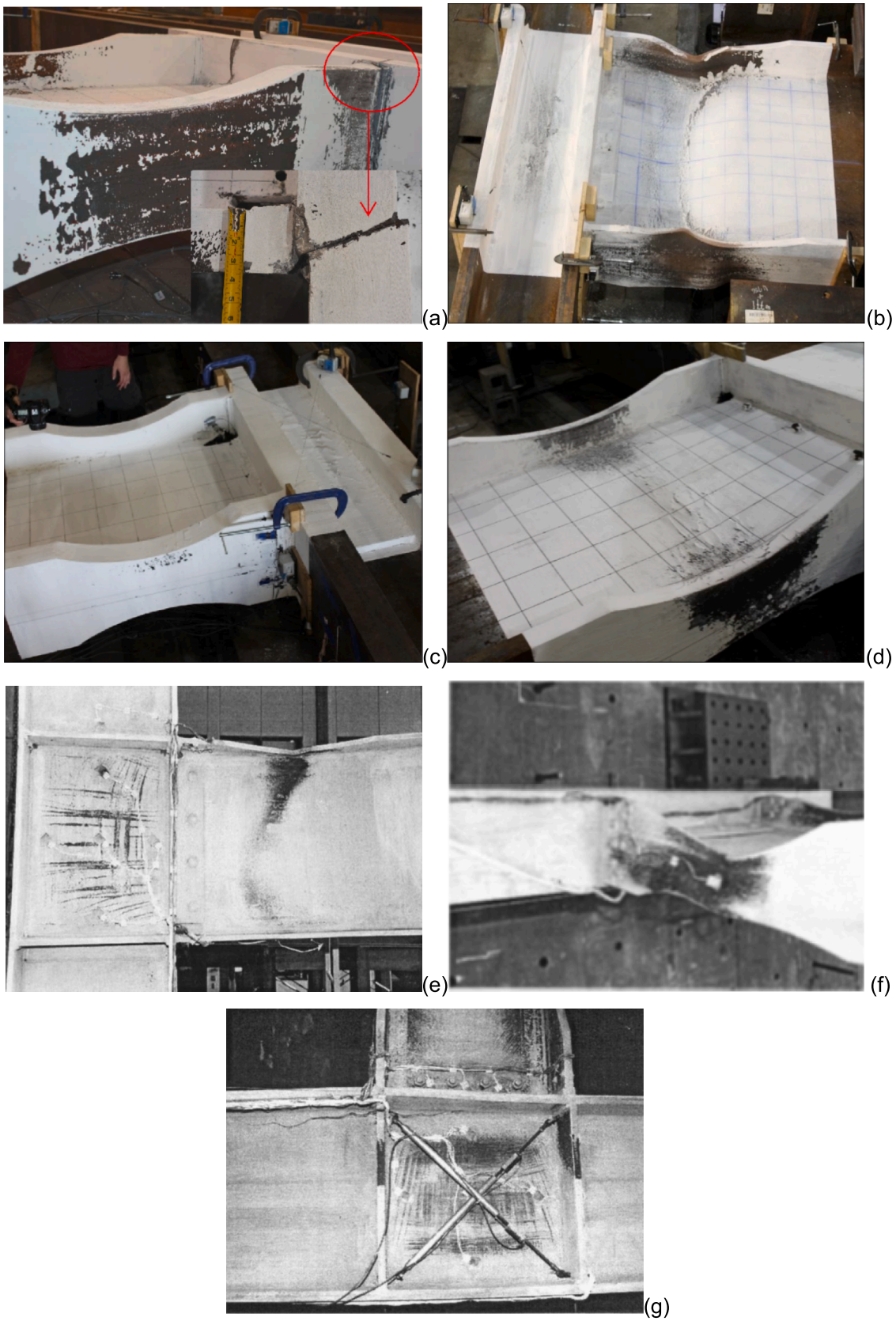


**Fig. 4.** Images of the test specimens in the plastic regime: a) SP1, b) SP2, c) SP3, d) SP4, e) DC1, f) DC2, g) DC3 (note: images of DC1, DC2, DC3 are from Chi and Uang, 2002 [24] ).

transverse flange directions. Inspection of the response indicated that the RBS contribution varied between 53 and 62 % of the connection deformation, whilst the column web panel contributed between 20 and 27 %. The remaining deformation was from the column elastic deformation. The test was stopped after fracture occurred during the second excursion of 170 mm (corresponding to 30 mrad).

SP2 failed by beam flexural yielding and inelastic local buckling, and achieved the desired deformation capacity as depicted in Fig. 3b. The *P-θ* response indicates typical flexural yielding and post-buckling degradation. Fig. 4b also shows the yielding patterns of SP2 at the end of the test. Yielding was followed by flange and web local buckling, as well as lateral out-of-plane buckling. Between 57 % and 90 % of the total rotation was concentrated at the RBS, with about 2–33 % contribution from the column web PZ.

For SP3, as shown in Fig. 4c and compared to other specimens, yielding was mostly concentrated in the PZ, with evident yielding observed in the doubler plates. Limited yielding developed at the RBS center, and no local buckling was observed. The test was stopped shortly after completing one full cycle of 4 % story drift, due to fracture of the weld at the bottom flange of the beam and the column flange, similar to SP1 (Fig. 3c). The relatively brittle fracture mode for SP1 and SP3 was attributed to the extreme demands on the relatively thick welds, for which conventional design procedures may substantially underestimate the local strain demands under cyclic loading [33].

For Specimen SP4, the PZ and RBS contributed in the ranges of 0–11 % and 71–83 %, respectively, to the connection deformation. The response was characterized by beam flexural yielding and inelastic local buckling (Fig. 4d), while achieving a significant deformation capacity. The test was stopped after two cycles at 230 mm, corresponding to 40 mrad due to significant column twist and failure of the lateral bracing (Fig. 3d). As a result of lateral bracing failure, the deep W40 column twisted, pushing the RBS out of plane. Because the RBS in Specimen SP4 was behaving well, like SP2, it is expected that SP4 would have been capable of much larger beam rotations if there were lateral bracing outside the RBS. Specimens SP2 and SP4 satisfied the current SMF qualification criteria per AISC seismic provisions [31], maintained moment strength above required levels, exceeded the required story drift, and did not experience fracture at the welds.

#### 2.2.2. DC1-3

The test results indicated that Specimen DC1 was characterized by initial PZ yielding, followed by web local buckling at the RBS, lateral torsional buckling, and local buckling at the compressed flange. The yielding of the doubler plate did not extend outside the boundaries of the PZ. The column experienced out-of-plane bending and torsion, unlike in more typical compact column cross-sections (Fig. 4e). This behavior largely results from the RBS buckling laterally and introducing torsion in the column, which becomes more evident for deep members. As shown in Fig. 3e, the rotation at peak force was 14 mrad, and around 30 mrad at 20 % reduction of force from the peak.

Specimen DC2 had a similar response, characterized by PZ yielding, web buckling, lateral torsional buckling, and local buckling of the flange at the RBS (Fig. 4f). Similar to DC1, the column of DC2 also experienced torsion and out-of-plane bending. As depicted in Fig. 3f, this occurred at 19 mrad rotation, whilst the rotation at 20 % reduction of load in the post-peak regime exceeded 30 mrad. For this specimen, the PZ contributed about 17 % to the total deformation.

The column twisting and out-of-plane bending of DC3 was followed by brittle failure within the PZ with a crack that propagated through the continuity plate into the column web below the beam (Fig. 4g). As shown in Fig. 3g, the specimen did not show any post-peak softening before brittle fracture occurred, indicating lower buckling amplitudes compared with the other two specimens. The rotation at fracture and test end was around 36 mrad, corresponding to a story drift that is below the AISC 341–16 limits for qualification. The contribution of the PZ to the total rotation was around 25 %.

## 3. Nonlinear validation

### 3.1. Modelling procedures

To obtain a detailed insight into RBS behavior with large member sizes, three-dimensional (3D) models of beam-column assemblages with RBS connection were constructed and analyzed using the non-linear finite element (FE) program ABAQUS [41]. Eight-node reduced integration brick elements (referred to as C3D8R in ABAQUS) were used in all models. Extruded solid elements from W sections representing the columns were connected to the beams using tie constraints. Particular attention was given to the RBS region and the column PZ by considering the measured dimensions from the experimental specimens [24,29].

The specimens, including the four stub elements made of W sections used as boundary conditions, were modelled together as illustrated in Fig. 5. At supports, the exterior faces of the W profile were connected to reference points, assigned with pinned boundary conditions, by means of multi-point constraints. The reference points are created on the FE model for the application of loads or boundary conditions, while multi-point constraints are a feature that allows the user to link different nodes and degrees of freedom together in the analysis [41]. Surface-to-surface interactions were also assigned to the interface between the column element of the specimens and the stub elements. For specimens with doubler plates, separate parts made of C3D8R elements were constructed and tied to the column web panel (e.g. see the modelling detail of Specimen DC1 depicted in Fig. 5). The number of elements and nodes varied between 51330 and 105629, and 74937 and 138011, respectively. The time associated with running the simulations was 1–3 h, depending on the size of the connection and level of inelastic deformations, as described in Section 3.2.

Cyclic displacements were applied to reference points at the actuator locations through constraints and transfer plates simulating the experimental loading history, with the ultimate applied displacement corresponding to the test end. Mesh sensitivity studies were also undertaken in order to capture accurately the inelastic strain propagation within the RBS as well as the local buckling effects. A fine mesh within the RBS and column PZ ($l_m$≈15-20 mm), combined with $l_m$≈30-40 mm outside of the critical regions, provided good agreement with tests as shown in the following sections. Using at least two mesh rows per flange thickness for relatively thin flanges (Specimens DC1-3) also provided a good balance in terms computational efficiency and accuracy in capturing local effects [42]. For specimens incorporating relatively thick flanges (Specimens SP1-4) a greater number of mesh rows per flange thickness were assigned to capture local buckling as shown in Figs. 5 and 6. This corresponds to an average flange thickness to element mesh size ratio of about 15.

The Newton-Raphson approach was adopted for the numerical integration procedure. The plastic multilinear kinematic hardening constitutive model available in the program was used to represent the steel material properties [41]. This was shown in previous studies to offer good representation of the monotonic and cyclic response of steel members and connections [43,44]. The material properties were obtained from coupon tests, separately for webs and flanges where possible, as depicted in Table 2. A bi-linear inelastic stress–strain curve with hardening, with an inelastic strain at peak strength ($f_u$) around 12 %, which is in the ranges expected for the steels from the tests in this paper, was used. Although the welds were not explicitly modelled, a mesh region corresponding with the physical location of the beam-to-column welds, was assigned nominal properties of the welding electrodes (Fig. 6). The mesh region with weld material properties had a length equal to around half of beam flange thickness.

### 3.2. Numerical results

The numerical results are summarized in Table 3, while the *P-θ* curves are depicted in Fig. 3. The force *P* was extracted from reference

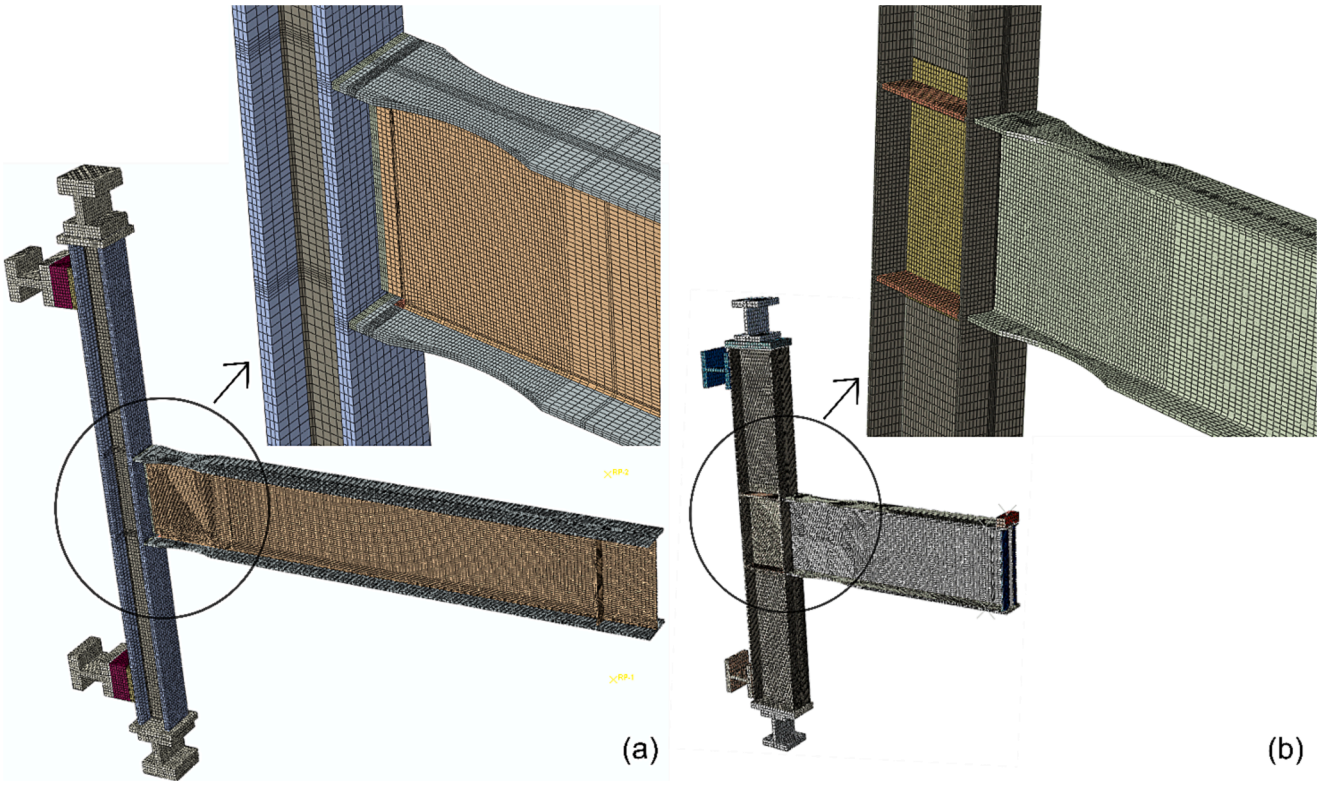


**Fig. 5.** Numerical models of: a) SP2, b) DC1.

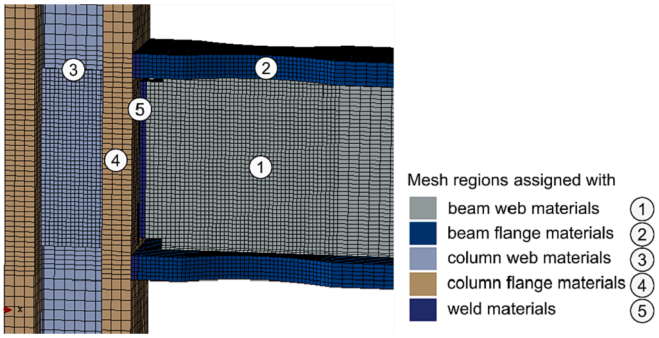


**Fig. 6.** Mesh details of SP3 specimen and material assignment.

points in the models, whilst $\theta$ was calculated using vertical displacements at the same point. The values of $P_y$, $\theta_y$, $P_u$ and $\theta_u$ were evaluated as described in Section 2. The results in Fig. 3e-g indicate that the stiffness, yield strength and overall hysteretic response were predicted with reasonable accuracy. The close-up views of the connection regions in the tests, shown in Fig. 4, and of the numerical von Mises strain maps, shown in Fig. 7, indicate that the analysis captures the experimental ultimate response.

The moment-rotation ($M$-$\theta$) envelopes in Fig. 8 also provide a direct experimental–numerical comparison in terms of the stiffness, strength, and post-peak response. The test bending moments ($M$) were assessed at the face of the column using loads recorded from the actuators multiplied by the lever arm corresponding to the centerline of the resistant forces. In the simulations, the moments ($M$) were assessed by dividing the reaction force at the reaction point by the corresponding lever arm. The test chord rotations ($\theta$) were assessed using test displacements recorded by string potentiometers located near the beam end after adjusting for the rigid body motion, whilst $\theta$ from simulations were assessed at the reaction point. As noted before, the chord rotations $\theta$ include all sources of deformations in an RBS connection, i.e. at the reduced section, panel zone, and the column. Detailed assessment of the experimental results and observations from the two test series, as well as comparisons and findings from the numerical simulations, are provided in the following subsections.

### 3.2.1. SP1-4

Comparison with the test results indicate that the analysis provides an accurate representation in terms of stiffness, yield strength and overall hysteretic response of SP1-4 as shown in Fig. 3a-d and 8a [46]. As shown in Fig. 7a-l, depicting the von Mises stress fields corresponding with yield rotation ($\theta_y$), ultimate rotation at the maximum moment ($\theta_u$) and maximum rotation ($\theta_{max}$), the stress distributions indicate: (i) yielding in RBS of SP1 with significant inelastic strains at the column face and yielding at the column PZ (Fig. 7a-c), (ii) yield at RBS, column face and PZ, followed by flange buckling at RBS with a lower damage at PZ for SP2 (Fig. 7d-f), (iii) yield at column face, PZ and RBS, followed by concentration of stresses at column face and PZ with limited yielding RBS flanges of SP3 at $\theta_{max}$ (Fig. 7g-i), and (iv) symmetric response with yield at column face and PZ, followed by asymmetric stress distribution at RBS and PZ with out-of-plane column rotation for SP4 (Fig. 7j-l).

The numerical results also confirmed that the cyclic degradation of SP2 arises from local buckling at the RBS, whilst for SP4 local buckling was combined with column twist and web buckling. The RBS flanges of SP3 had lower stress levels than the remaining connection components, and there was no degradation at the RBS due to the absence of flange local buckling, but significant column web panel distortion occurred. SP1 represents an intermediate case as the model showed extensive yielding at the RBS. However, due to the relatively stocky flanges, local buckling did not occur, and the connection sustained significant hardening. The stresses transferred from the beam flanges facilitated stress concentrations at the column flange.

### 3.2.2. DC1-3

The numerical $P$-$\theta$ of DC1 captures very well the stiffness, strength

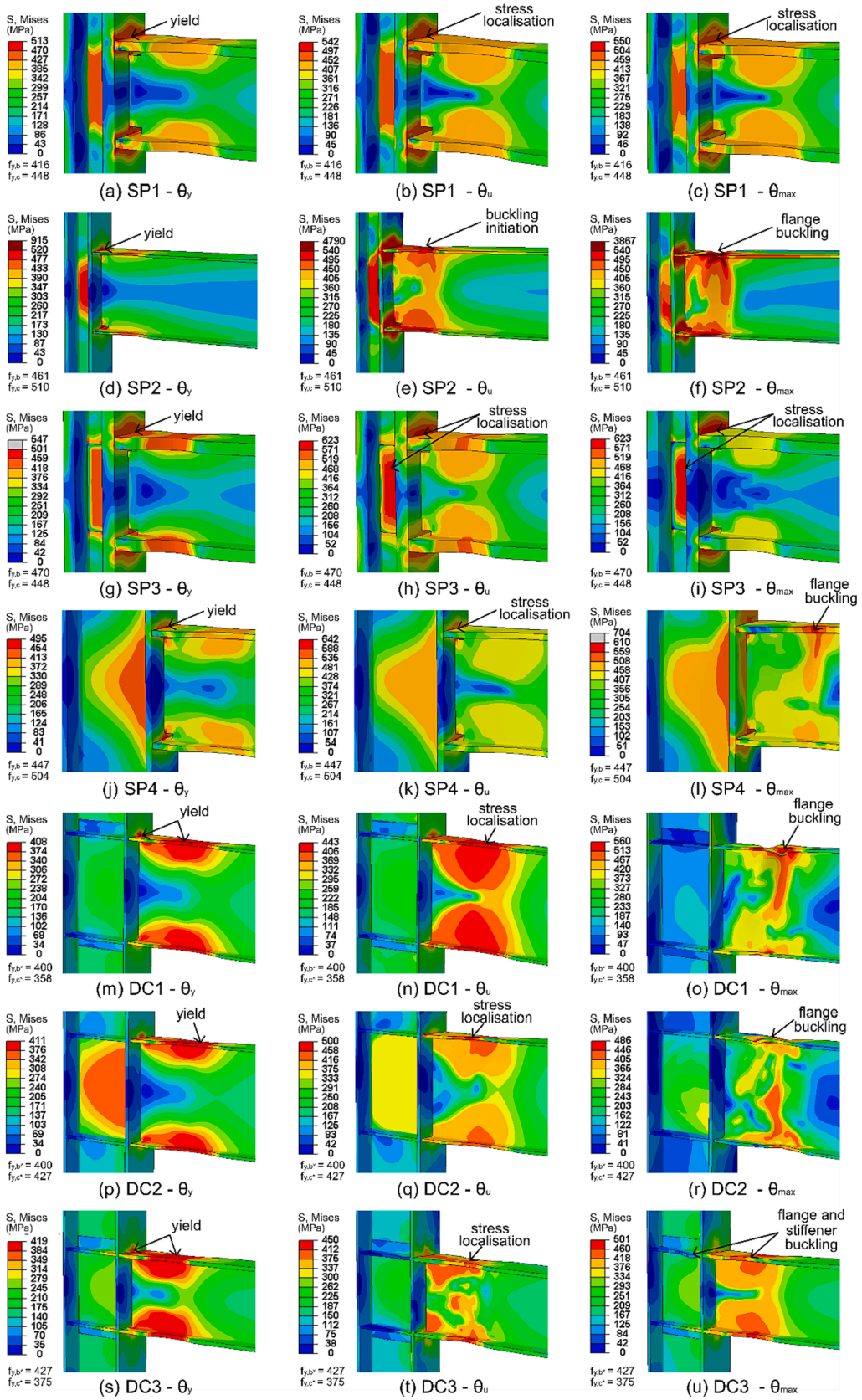


**Fig. 7.** Von Mises stress maps (labels for subplots are specimen size, then rotation level at which the maps were extracted: $\theta_y$ – yield, $\theta_u$ – ultimate corresponding with the maximum moment, $\theta_{max}$ – maximum rotation achieved, *indicate flange yield strengths, see Table 2 for details).

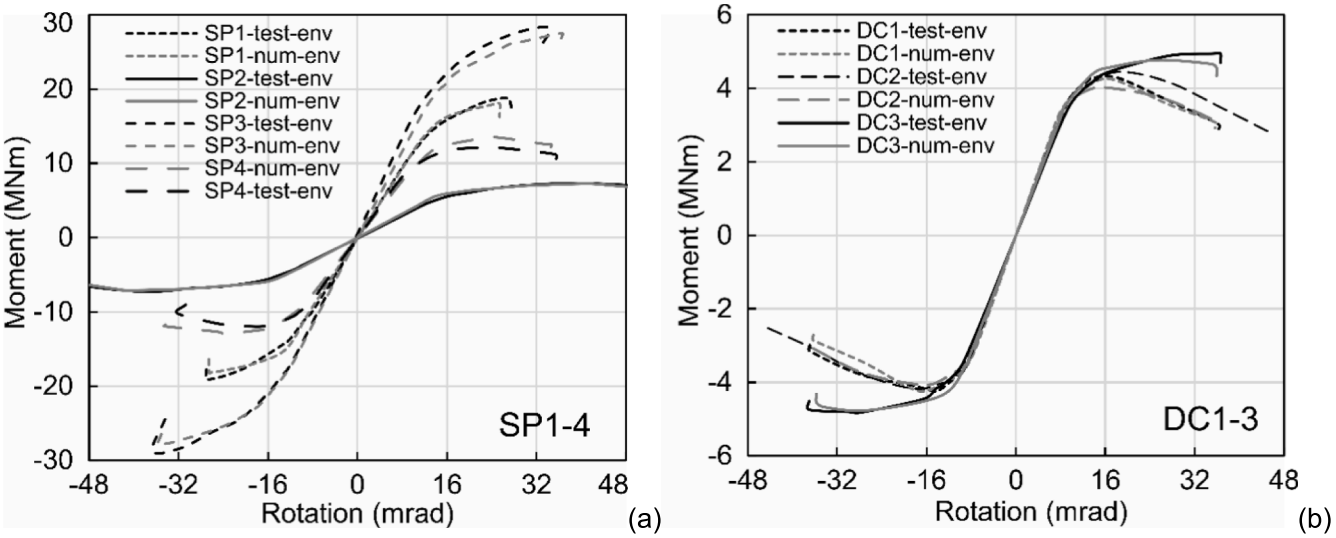


**Fig. 8.** Comparative moment - rotation curves (M-θ) for a) Specimens SP, b) Specimens DC.

and inelastic degradation observed in tests (Fig. 3e). The stress maps in Fig. 7m-o indicate that yield at RBS and column face, with the stresses localization at the RBS governing the response. This suggests that the demands on the welds were relatively low and weld fracture would not occur, as confirmed by the tests (Fig. 4e). The uneven stress distribution at the column flange above the beam corresponds to column twist due to the instability at the RBS.

The comparative *P-θ* curves of Specimen DC2 in Fig. 3f show very good agreement with the tests in terms of stiffness, strength, hysteresis, and post-peak degradation. Compared to DC1, the stress maps in Fig. 7p-r show higher levels of stress in the PZ, as expected since DC2 did not have doubler plates unlike DC1. The ultimate behavior is well captured by the DC1 and DC2 models, which show flange buckling at the RBS and an uneven stress distribution in the column. The latter resulted in column twisting and out-of-plane bending, which is also shown in Fig. 4f.

The stiffness, yield point, peak strength, and hysteresis of Specimen DC3 are well captured by the simulations (Fig. 3g). As shown in Fig. 7s-u, inelastic deformations were concentrated mostly at the RBS. The top continuity plate was bent and there was some stress localization at the connection with the column flange adjacent to the beam indicating likelihood of fracture as occurred in tests (Fig. 4g). The stress maps indicate stress concentrations of similar magnitude at the column face and at the RBS, implying high demands at the beam-column welds.

Having gained confidence in the numerical procedures employed in this investigation through the validations of the test results from seven specimens from two distinct test series, further parametric studies on thirty models with jumbo sections, are described in subsequent sections of this paper. As shown in Fig. 2a,b, the sizes of the connection components from the first series, represented by grey triangles, are larger in comparison to the existing tests which are shown in grey circles and black diamond markers [25]. The additional numerical models, which are outside the prequalification limits are shown in black squares in Fig. 2a,b.

## 4. Ultimate response characteristics

As discussed in Section 2, Specimens SP1 and SP3 had an ultimate behavior governed by fracture at the welds, whilst in SP2, SP4, DC1, DC2 and DC3 deterioration occurred due to local flange buckling. Specimens SP4 and DC3 also developed out-of-plane bending, which for the latter led to PZ fracture. In the models, the welds were not explicitly represented, but a mesh region of half the beam flange thickness consisting of flange and web elements. This mesh region was located in the beam at the column face, and the corresponding mesh elemenets were assigned nominal properties of the welding electrodes. To estimate fracture, existing analytical procedures are employed and compared with SP1 and SP3 tests. Critical buckling strains are also assessed to obtain the governing response mode as discussed below.

### 4.1. Cyclic fatigue

#### 4.1.1. Ultra-low cycle fatigue response

The cyclic fatigue behavior of steel under<100 large-amplitude inelastic cyclic loading can be generally strain-represented [47,48]. This fatigue regime can be referred to as ultra-low-cycle fatigue and has distinctive damage mechanisms compared to those occurring under low-cycle fatigue [52,53]. Many models for predicting the ultimate fatigue response of welded connections essentially employ the Coffin–Manson (CM) [49,50] strain-life model. The CM model assumes that the plastic strain decreases linearly with the number of reversals in a log–log scale: $(\Delta\varepsilon_p/2) = \varepsilon_f'(2N_f)^c$, where $\Delta\varepsilon_p/2$ is the plastic strain amplitude, $\varepsilon_f'$ is the fatigue ductility coefficient, $c$ is the fatigue ductility exponent, and $2N_f$ is the number of reversals to failure. A CM relationship can be calibrated for a specific connection detail with set member sizes and materials but is not applicable if the detailing or materials change as the ultra-low cycle fatigue fracture is dependent on the triaxiality ratio, plastic strain rate of the material and to a lesser extent on the Lode angle [51–53].

The CM method does not address the damage mechanisms initiating the failure nor includes explicitly any damage evolution processes, it does not have the capability to predict failure outside the experimentally investigated range, and usually requires different curves for different loading conditions. Unless the effect of triaxiality is considered in ultra-low cycle fracture assessments, the application of a conventional CM model is likely to overestimate the predicted strain life for multiaxial stress cases [54]. The influence of triaxiality on the CM relationship can be considered by fitting CM function parameters against test and numerical results on coupon and circular notched samples [54].

Iyama and Ricles (2009) [55] proposed a model which can predict the crack length at failure based on the equivalent plastic strains and triaxiality ratio, obtained from nonlinear simulations at various locations of the connection. In this model, the equivalent plastic strain obtained from simulations is used to predict crack length at failure, which is directly related to $N_f$. Although in most structural engineering applications the crack initiation is used as a performance criterion, determining crack propagation under complex stress states is essential to

understand the response of structural members under various loading regimes. Simulating crack propagation requires the integration of fracture criteria along with numerical schemes that can simulate this separation within finite-element models [52]. For example, phase-field based formulations can predict the propagation of cracks in metals exhibiting complex cyclic deformation and damage responses, by incorporating large-deformation modelling and combined nonlinear isotropic and kinematic hardening laws [56,57]. These approaches implicitly consider the influence of triaxiality on the fatigue life of the material.

#### 4.1.2. Stress triaxiality

The triaxiality T of the stress tensor is defined as the ratio of the volumetric stress over the effective (von Mises) stress, and defines the process of ductile fracture initiation, cyclic damage degradation and fracture strain ($\varepsilon_f$) [51,58]. At moderate ($0.33 \leq T \leq 0.75$) and high ($T > 0.75$) stress triaxiality, void growth is dominant in the process of ductile fracture initiation [60,61]. For moderate triaxiality, the cyclic damage degradation parameter decreases linearly with increasing $T$, while for high values of $T$ cyclic damage degradation grows proportionally with $T$. For structural steels, the microscopic damage mechanism changes from microvoid elongation to microvoid dilation at $T = 0.75$ which corresponds to the maximum fracture strain that can be reached by the material [61]. The fracture strain increases by a factor of 1.6 from $T = 0$ to $T = 0.75$, and then decreases gradually with $T$ and is slightly influenced by the Lode angle (Fig. 9a) [62,63].

To support the assessments carried out in this section, the T developed in the main connection components of SP1-4 and DC1-3 models were determined from simulations. The connection components at which the $T$ was assessed are the center of the reduced beam section (RBS), welds at the column face (W), center of panel zone (PZ), and in column flange (CF) at the connection to the beam flange. It was observed that $T_{RBS} = 0.35$–$0.51$ at RBS, $T_W = 0.98$–$1.73$ at W, TCF = 0.83–1.83 at CF, and $T_{PZ} = 0.05$–$0.69$ at PZ, with corresponding averages of $T_{RBS} = 0.43$, $T_W = 1.35$, $TCF = 1.33$ and $T_{PZ} = 0.37$, respectively. These ranges are depicted in Fig. 9a. As indicated by the average ratios, the triaxiality is of similar magnitude by pairs (i.e. RBS and PZ, and W and CF), and within ranges reported in the literature ($T = 1.0$ for welded beam-to-column, and $T = 0.4$ for RBS connections [59]).

Fig. 9a shows a typical relationship between the $T$ and $\varepsilon_f$ for structural steels. Assuming that the maximum $\varepsilon_f$ can be achieved by the material is at $T = 0.75$, for $T \approx 1.0$ that is typical for welded steel beam-to-column connections, the fracture strain is reduced by 30 %. Previous studies showed that at moderate stress triaxiality, the prediction accuracy of conventional CM model is acceptable, confirming the validity of CM for these ranges [54]. Assuming a value of $T = 0.75$ as the upper bound of moderate triaxiality and that the maximum fracture strain can be achieved at this $T$ level (Fig. 9a), a reduction factor can be applied to the CM strain life function to capture the influence of triaxiality on the plastic strain life. In this paper, the CM parameters were multiplied by the minimum reduction factor $\lambda_{f,\min}$ shown in Fig. 9a to account qualitatively for the influence of stress triaxiality on ultimate conditions.

#### 4.1.3. Ultra-low cycle fatigue plot

To assess the governing response mode of RBS connections, the Coffin-Manson model, in the form of $(\Delta\varepsilon_p/2) = \varepsilon_f'(2N_f)^c$ was used (Fig. 9b). For this, the plastic strain is replaced by the equivalent plastic strain, referred to as PEEQ in ABAQUS [41], denoted here as $\xi$, as obtained from the analysis [55]. The development of equivalent plastic strains at RBS and W of SP1 model are schematically shown in Fig. 9b, against the number inelastic cycles each component was subjected to. As yielding initiated at W at the column face significantly earlier than at the RBS, the inelastic cycles for W are greater than for RBS.

In the absence of fatigue test data, the fatigue ductility coefficient ($\varepsilon_f'$) and exponent ($c$) considered herein were obtained from the literature based on tests on structural steels similar to those used in this experimental investigation [48,64–67]. The samples adopted for assessing these coefficients were either flat coupons [48,65], round notch specimens [66,67], or welded plate cross specimens [64]. For coupons, the specimen geometry and testing procedures followed the ASTM E606 recommendations [68]. The fatigue ductility coefficient $\varepsilon_f'$ varied between 0.450 and 0.747 and the fatigue ductility exponent $c$ between −0.664 and −0.529. The average $\varepsilon_f'$ is 0.567 and the average $c$ is −0.601. In Fig. 9b, the CM relationships associated with coefficients from each of the above studies are represented in black dashed lines, whilst the average CM relationship by a red continuous line. As noted above, to qualitatively account for stress triaxiality in the plastic strain life, the CM relationship is represented by $\lambda_{f,\min}$. This is shown by the dashed red line in Fig. 9b, and serves the purpose of indicating ranges at which fracture may occur. As noted above, this approach is intended to provide only a qualitative prediction of where and when fracture might occur [69].

### 4.2. Local flange buckling

When relatively strong PZs are employed, the failure of RBS connections can develop either due to inelastic local buckling of the compressed flange, or by fracture at the welds. The approaches described above can be used to assess the ultimate condition in tension, whilst the

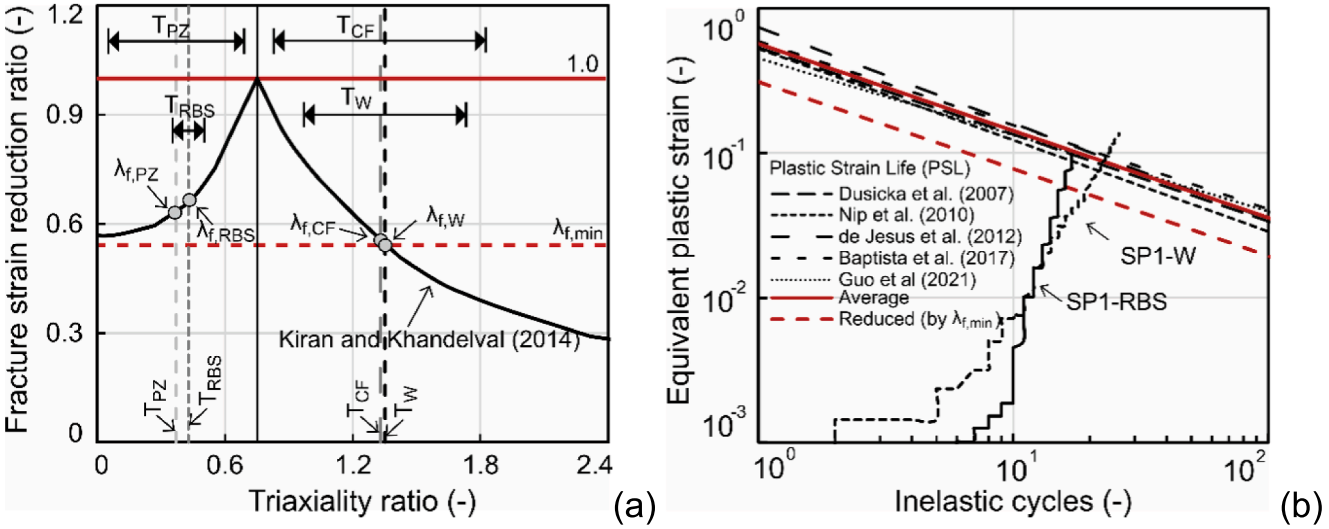


**Fig. 9.** a) The influence of triaxiality ratio on the fracture strain, b) Comparative ultra-low cycle fatigue plot,

local flange buckling can typically be estimated using the critical buckling strain $\varepsilon_{cr}$. This is the ratio between $k \times \pi^{2\times}E \times \varepsilon_y$ and $12 \times f_y\times(1\text{-}\nu^2)\times(b/t)^2$, in which the coefficient $k$ depends on the boundary conditions and aspect ratio of the loaded plate, $E$ is the elastic modulus, $\varepsilon_y$ is the yield strain, $f_y$ is the yield strength, $\nu$ is Poisson ratio, $b$ is the width of the plate and $t$ is its thickness [70]. Evaluation of local buckling based on the above criterion, initially derived from elastic plate buckling and extended to represent inelastic strains, can be used as a relative measure to assesses the likelihood of buckling. This approach was widely used for predicting the failure of structural steel elements as it was extensively calibrated empirically for simplicity in many studies in the literature, against inelastic local buckling test results [71,72].

In RBS connections, local buckling occurs within the reduced section in the form of a half wave, which largely corresponds to the cut length (Figs. 6 and 7). In this study, the aspect ratio of the flange is considered as the ratio between the RBS cut length and the average outstanding flange width. Based on this assumption, for the test specimens in Section 2, the aspect ratio varied in the range of 4.52–7.19. For an idealized flat plate element subjected to compression, which is assumed to be fixed along one edge, i.e. connection with the web, and free along the other edge, the elastic buckling coefficient is $k = 1.277$ [73]. Theoretically, this coefficient is $k = 0.425$ for a plate simply supported along one edge and free along the other edge.

The actual support condition however depends on the relative stiffness of the web and flange. For typical hot rolled sections, this coefficient is typically considered as $k = 0.7$–$1.0$ [32,72,74]. However, for large steel sections such as those in SP1 and SP3, the web may be relatively more rigid than for typical hot rolled sections and $k > 1.0$ may apply. Note that these factors represent a lower bound and are associated with constant compression stress in the flanges, whilst for non-constant stress distribution, the factors can be significantly higher by a factor of 2.5 [75]. As in the case of the ultra-low cycle fatigue assessments, to indicate the ranges of strain at which local bucking may occur, both $k = 0.7$ and $k = 1.227$ are considered herein. These are depicted by green dashed and continuous curves, respectively, in Fig. 10. This figure depicts the relationship between the number of inelastic cycles and the equivalent plastic strain development $\xi$ [55]. As shown in the figure, k = 0.7 provides the best estimates, as it may be most representative for the

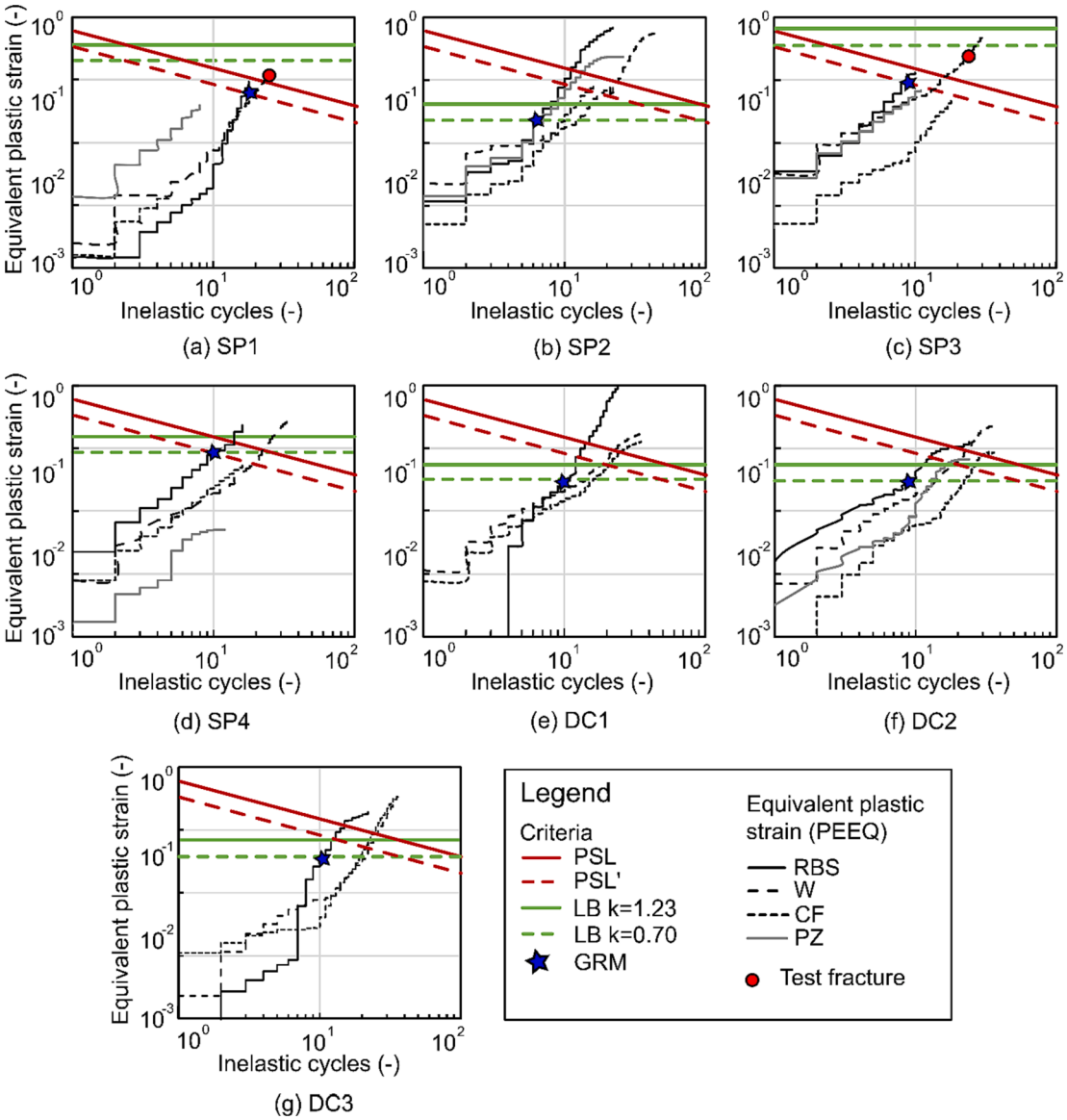


**Fig. 10.** Ultra-low cycle fatigue plot for Specimens: a) SP1, b) SP2, c) SP3, d) SP4, e) DC1, f) DC2, g) DC3 (Notations: PSL – plastic strain life using average CM parameters, PSL' – translated PSL using $\lambda_{f,min}$, CM – Coffin Manson, LB – local buckling, GRM – governing response mode, RBS – reduced beam section, W – welds, CF – column face, PZ – panel zone).

relative stiffness of the plated components of the sections investigated in this paper.

### 4.3. Plastic strain development

The equivalent plastic strains $\xi$ in Fig. 10, as obtained from the numerical simulations of the test specimens, are shown for the main connection components: center of the reduced beam section (RBS), welds at the column face (W), center of panel zone (PZ), and in column flange (CF) at the connection to the beam flange. As noted above, the abscissa plots the number of inelastic cycles which each connection components were subjected to. The figure also indicates: (i) plastic strain life (PSL) estimates based on the average CM relationship and translated lower bound CM relationship as described above (represented by inclined red continuous and dashed lines, respectively), and (ii) critical buckling strain (LB) (horizontal green continuous and dashed lines, respectively).

A direct comparison between the development of equivalent plastic strains $\xi$ at different connection zones versus number of inelastic cycles indicate the main critical regions as well as the susceptibility to fracture at the welds. For $\xi = 0$, the material is in the elastic regime, whilst $\xi > 0$ indicates that the material yielded. As shown in Fig. 10a for SP1, the strains at the RBS and W are largely of the same magnitude and similar gradient. Some inelastic strains are observed at CF and PZ. Both curves intersect the plastic strain life (PSL) curve at a similar number of cycles, and prior to local buckling (LB) occurring (i.e. the intersection point between $\xi_W$ and $\xi_{RBS}$ with PSL curve below the LB line). It is suggested that the intersection of $\xi_W$ with PSL can provide an indication of potential weld fracture, and is referred to as the governing response mode (GRM) in Fig. 10a.

For SP2, shown in Fig. 10b, the $\xi$ development at RBS and PZ has a similar gradient and magnitude indicating a balanced contribution of the two components to the joint response, whilst W and CF have a smaller gradient. More importantly, the LB curve intersects $\xi_{RBS}$, governing the response, before $\xi_{RBS}$ intersects the PSL curves. This behavior is in agreement with experimental observations, load-rotation curves, and strain maps in Fig. 5b and 7b, respectively. The same behavior is captured in Fig. 10e,f,g for Specimens DC1-3. In all situations, LB intersects $\xi_{RBS}$ before any other form of failure is likely to develop within the connection (e.g. PZ fracture for DC3).

The large $\xi_{PZ}$ shown in Fig. 10c for SP3 corresponds with the stress distribution from Fig. 7g-i, indicating similar concentration at the PZ, W and RBS. Although the $\xi_{RBS}$ curve intersects first the PSL line, this is in the vicinity of $\xi_W$ curve. By looking at the $\xi_W$ and $\xi_{RBS}$ of SP1 and SP2 in Fig. 10a and 10b, respectively, the equivalent plastic strain development in SP3 is more similar to SP1 than SP2. Most importantly, the LB curves in Fig. 10c are above the intersection between the PSL curve and any $\xi$, indicating that fracture in one of the connection components is likely. This is in agreement with the observations from the test, which was stopped due to fracture. Ultimately, for SP4 the lower LB curve in Fig. 10d is close to the lower PSL curve and the intersection with the governing $\xi$ (RBS), indicating that weld fracture was not imminent as the intersection between $\xi_{RBS}$ with PSL occurs before the intersection with $\xi_W$. This is supported by the relatively low buckling amplitudes shown in Fig. 4d, and the very low stress localizations at the welds as well as the out-of-plane bending shown in Fig. 7j-l.

Based on the above observations, it is suggested that by considering the $\xi$ development at various connection components in conjunction with PSL and LB criteria, the governing response mode (GRM) and likelihood of weld fracture can be estimated, but only in conjunction with the overall load or moment-rotation curves and joint strain maps. This approach is used as a measure to assess the likelihood of fracture in the connections investigated in the parametric study described below.

## 5. Parametric assessments

To obtain a detailed insight into the behavior of large beam-column connections incorporating RBS, 30 models were constructed (Table 4) with sections outside the test database. Twenty connections (M1-M20) designed to the current codes (neglecting member size limits) had sections within the ranges of test specimens from Section 2, but outside of the prequalification ranges (see the square markers in Fig. 2a,b). In these connections, the yield strength of the steel in the beam and column were $f_{y,0.2\%}$=345 MPa, and $f_{y,0.2\%}$=450 MPa, respectively. The parameters defining the geometry of the RBS cut were kept constant (Table 4). The remaining 10 models (Models SP1-*P1* to SP3-*P5*) were derived from the geometry of Specimens SP1 and SP3, in which the position and depth of the RBS cut were changed incrementally, hence the $M_{RBS}/M_{beam}$ ratio varied whilst the column moment capacity $M_{col}$ was constant. For the SP parametric models, the material properties were kept identical to those from Table 2. For all models, the same procedures described in Section 3, were adopted. To limit out-of-plane deformations and column twist, lateral restraints were provided to the beams at the location of the beam end stiffener shown in Fig. 5a. In all models, an initial monotonic load-deformation response was obtained, from which the yield displacement was determined and used to construct the cyclic displacement protocol [45], primarily to reduce the number of cycles in the elastic regime and save computational time. In addition to the moment – rotation ($M$-$\theta$) curves obtained from simulations, plastic strain distributions at the main connection components were also compared.

### 5.1. Overall behavior

Fig. 11 illustrates the typical moment-rotation ($M$-$\theta$) curves for selected models from Table 4, representative of different types of behavior, whilst Fig. 12 shows the von Mises stress maps for all 20 models (M1-M20). As defined in Section 3, bending moments ($M$) were assessed at the face of the column using forces extracted from reaction points, whilst the chord rotations ($\theta$) were calculated from the displacement at the same points, divided by the distance to the column face. In addition to the monotonic and cyclic $M$-$\theta$ curves, the rotation at which the largest equivalent plastic strain intersects the governing criteria (PSL or LB) is identified as the governing response mode (GRM) and is also indicated in the figures. As indicated in Fig. 12, which depicts stress maps at rotation levels beyond GRM, a number of distinct responses are obtained:

i. significant local buckling at the RBS in conjunction with largely elastic deformations at the PZ, column flange (CF), and column face in the welds (W) (M1, M2, M3, M5)
ii. significant local buckling at the RBS in conjunction with limited inelastic development at the CF, PZ or W (M4, M5, M6)
iii. Limited (M9, M10, M11) or significant (M7, M12, M15, M16) local buckling at the RBS alongside some inelastic deformations at the CF, PZ, or W
iv. Low amplitude local buckling at the RBS, significant inelastic strain in the PZ and large inelastic deformations at W and CF (M13, M14)
v. Large deformations at the W, CF and PZ, twist of the deep column section and yielding at the RBS (M8, M17, M18, M19, M20)

As shown in Figs. 11 and 12 and Table 4, Model M4 had a moment-rotation (M-θ) characterized by hardening, local buckling at RBS, and reaching over $\theta_u > 35$ mrad joint rotation. The ultimate rotation $\theta_u$ corresponds to the maximum moment obtained from the cyclic M-θ curves to GRM as indicated in Fig. 11. Both compact (M4) and deep (M18) sections exhibited a desirable behavior. The $M$-$\theta$ curves of M7 and M8 are similar with $\theta_u > 35$ mrad. The response of both connections was stable up to this level of $\theta_u$, however, further cycling beyond GRM would have produced local buckling at the RBS in M7 and column twisting in

**Table 4**
Parametric assessment.

| Model | Column section (-) | Beam section (-) | $a/b_f$ (-) | b/d (-) | $c/b_f$ (-) | a (mm) | b (mm) | c (mm) | $M_y$ (MNm) | $M_u$ (MNm) | $\theta_y$ (mrad) | $\theta_u$ (mrad) | $\mu_\xi$ (-) | $\lambda_M$ (-) |
|---|---|---|---|---|---|---|---|---|---|---|---|---|---|---|
| M1 | W14 × 873 (W 360 × 410 × 1299) | W33 × 152 (W 840 × 295 × 226) | 0.63 | 0.75 | 0.20 | 266 | 724 | 85 | 2.4 | 2.7 | 9.0 | 30.2 | 0.20 | 0.26 |
| M2 | W14 × 873 (W 360 × 410 × 1299) | W36 × 361 (W 920 × 420 × 537) | 0.63 | 0.75 | 0.20 | 266 | 724 | 85 | 6.8 | 7.7 | 10.4 | 23.3 | 0.46 | 0.26 |
| M3 | W14 × 808 (W 360 × 410 × 1202) | W36 × 361 (W 920 × 420 × 537) | 0.63 | 0.75 | 0.20 | 266 | 724 | 85 | 6.6 | 8.3 | 9.9 | 32.1 | 0.42 | 0.29 |
| M4 | W14 × 730 (W 360 × 410 × 1086) | W36 × 361 (W 920 × 420 × 537) | 0.63 | 0.75 | 0.20 | 266 | 724 | 85 | 6.7 | 8.4 | 10.8 | 36.1 | 0.54 | 0.32 |
| M5 | W14 × 730 (W 360 × 410 × 1086) | W36 × 302 (W 920 × 420 × 449) | 0.63 | 0.75 | 0.20 | 264 | 711 | 85 | 5.8 | 6.8 | 11.6 | 32.3 | 0.43 | 0.27 |
| M6 | W14 × 665 (W 360 × 410 × 990) | W36 × 361 (W 920 × 420 × 537) | 0.63 | 0.75 | 0.20 | 266 | 724 | 85 | 6.9 | 8.9 | 12.1 | 51.7 | 0.52 | 0.36 |
| M7 | W14 × 550 (W 360 × 410 × 818) | W36 × 302 (W 920 × 420 × 449) | 0.63 | 0.75 | 0.20 | 264 | 711 | 85 | 5.5 | 6.7 | 11.4 | 41.4 | 0.97 | 0.38 |
| M8 | W40 × 593 (W 1000 × 400 × 883) | W44 × 408 (W 1100 × 400 × 607) | 0.63 | 0.75 | 0.20 | 256 | 854 | 82 | 9.4 | 10.5 | 12.3 | 35.1 | 0.93 | 0.24 |
| M9 | W14 × 730 (W 360 × 410 × 1086) | W36 × 318 (W 920 × 310 × 474) | 0.63 | 0.75 | 0.20 | 198 | 728 | 63 | 5.9 | 7.1 | 11.0 | 36.1 | 0.45 | 0.25 |
| M10 | W14 × 873 (W 360 × 410 × 1299) | W36 × 387 (W 920 × 310 × 576 | 0.63 | 0.75 | 0.20 | 201 | 745 | 64 | 7.3 | 8.9 | 10.9 | 35.6 | 0.58 | 0.25 |
| M11 | W14 × 873 (W 360 × 410 × 1299) | W36 × 387 (W 920 × 310 × 576) | 0.63 | 0.75 | 0.20 | 201 | 745 | 64 | 7.5 | 8.8 | 11.9 | 32.4 | 0.55 | 0.41 |
| M12 | W14 × 873 (W 360 × 410 × 1299) | W36 × 441 (W 920 × 420 × 656) | 0.63 | 0.75 | 0.20 | 269 | 740 | 86 | 8.5 | 10.3 | 10.8 | 32.2 | 0.60 | 0.44 |
| M13 | W14 × 873 (W 360 × 410 × 1299) | W36 × 529 (W 920 × 420 × 787) | 0.63 | 0.75 | 0.20 | 273 | 758 | 87 | 10.8 | 12.1 | 12.6 | 32.4 | 0.73 | 0.47 |
| M14 | W14 × 873 (W 360 × 410 × 1299) | W36 × 723 (W 920 × 420 × 1077) | 0.63 | 0.75 | 0.20 | 282 | 796 | 90 | 14.8 | 20.1 | 12.5 | 25.0 | 1.11 | 0.60 |
| M15 | W14 × 808 (W 360 × 410 × 1202) | W40 × 372 (W 1000 × 400 × 554) | 0.63 | 0.75 | 0.20 | 255 | 774 | 82 | 7.7 | 9.2 | 11.7 | 36.4 | 0.55 | 0.31 |
| M16 | W14 × 808 (W 360 × 410 × 1202) | W40 × 397 (W 1000 × 400 × 591) | 0.63 | 0.75 | 0.20 | 256 | 780 | 82 | 8.5 | 9.4 | 12.9 | 35.3 | 0.66 | 0.33 |
| M17 | W36 × 925 (W 920 × 420 × 1377) | W36 × 387 (W 920 × 310 × 576) | 0.63 | 0.75 | 0.20 | 201 | 745 | 64 | 7.6 | 8.7 | 11.1 | 32.3 | 0.49 | 0.12 |
| M18 | W36 × 925 (W 920 × 420 × 1377) | W36 × 441 (W 920 × 420 × 656) | 0.63 | 0.75 | 0.20 | 269 | 740 | 86 | 8.4 | 10.0 | 9.7 | 30.9 | 0.62 | 0.16 |
| M19 | W36 × 925 (W 920 × 420 × 1377) | W36 × 529 (W 920 × 420 × 787) | 0.63 | 0.75 | 0.20 | 273 | 758 | 87 | 9.1 | 12.3 | 8.4 | 35.7 | 0.73 | 0.19 |
| M20 | W36 × 925 (W 920 × 420 × 1377) | W36 × 723 (W 920 × 420 × 1077) | 0.63 | 0.75 | 0.20 | 282 | 796 | 90 | 12.6 | 18.1 | 10.5 | 45.3 | 1.07 | 0.26 |
| SP1-*P1* | W 36 × 652 (W 920 × 420 × 970) | W 14 × 873 (W 360 × 410 × 1299) | 0.50 | 0.85 | 0.18 | 223 | 887 | 80 | 12.5 | 19.1 | 11.0 | 36.3 | 1.44 | 0.52 |
| SP1-*P2* | W 36 × 652 (W 920 × 420 × 970) | W 14 × 873 (W 360 × 410 × 1299) | 0.50 | 0.85 | 0.25 | 223 | 887 | 112 | 12.0 | 17.0 | 11.0 | 36.3 | 0.22 | 0.43 |
| SP1-*P3* | W 36 × 652 (W 920 × 420 × 970) | W 14 × 873 (W 360 × 410 × 1299) | 0.33 | 0.85 | 0.25 | 147 | 887 | 112 | 11.7 | 16.8 | 11.0 | 36.3 | 0.63 | 0.38 |
| SP1-*P4* | W 36 × 652 (W 920 × 420 × 970) | W 14 × 873 (W 360 × 410 × 1299) | 0.33 | 0.85 | 0.33 | 147 | 887 | 147 | 11.1 | 13.7 | 9.8 | 37.5 | 0.31 | 0.30 |
| | | | 0.50 | 0.85 | 0.33 | 223 | 887 | 147 | 11.4 | 15.1 | 10.7 | 36.8 | 0.42 | 0.34 |

(*continued on next page*)

**Table 4** (*continued*)

| Model | Column section (-) | Beam section (-) | $a/b_f$ (-) | b/d (-) | $c/b_f$ (-) | a (mm) | b (mm) | c (mm) | $M_y$ (MNm) | $M_u$ (MNm) | $\theta_y$ (mrad) | $\theta_u$ (mrad) | $\mu_\xi$ (-) | $\lambda_M$ (-) |
|---|---|---|---|---|---|---|---|---|---|---|---|---|---|---|
| SP1-*P5* | W 36 × 652 (W 920 × 420 × 970) | W 14 × 873 (W 360 × 410 × 1299) | | | | | | | | | | | | |
| SP3-*P1* | W 36 × 925 (W 920 × 420 × 1377) | W 14 × 873 (W 360 × 410 × 1299) | 0.50 | 0.85 | 0.21 | 237 | 929 | 99 | 18.0 | 30.8 | 13.0 | 36.1 | 1.12 | 0.83 |
| SP3-*P2* | W 36 × 925 (W 920 × 420 × 1377) | W 14 × 873 (W 360 × 410 × 1299) | 0.50 | 0.85 | 0.25 | 237 | 929 | 118 | 18.7 | 29.1 | 14.1 | 35.1 | 0.99 | 0.76 |
| SP3-*P3* | W 36 × 925 (W 920 × 420 × 1377) | W 14 × 873 (W 360 × 410 × 1299) | 0.33 | 0.85 | 0.25 | 156 | 929 | 118 | 19.1 | 27.9 | 14.8 | 34.7 | 0.67 | 0.66 |
| SP3-*P4* | W 36 × 925 (W 920 × 420 × 1377) | W 14 × 873 (W 360 × 410 × 1299) | 0.33 | 0.85 | 0.33 | 156 | 929 | 156 | 17.3 | 25.2 | 14.3 | 35.1 | 0.71 | 0.52 |
| SP3-*P5* | W 36 × 925 (W 920 × 420 × 1377) | W 14 × 873 (W 360 × 410 × 1299) | 0.50 | 0.85 | 0.33 | 237 | 929 | 156 | 17.3 | 25.5 | 14.5 | 34.9 | 0.72 | 0.60 |

Note: 1) the section types are first defined in the imperial system and then in the metric system (in brackets); 2) the last term in the column and beam section definition represents the weight of the profile; e.g for W 36 × 652 (W 920 × 420 × 970), the weight is 652 lb/ft (970 kg/m).

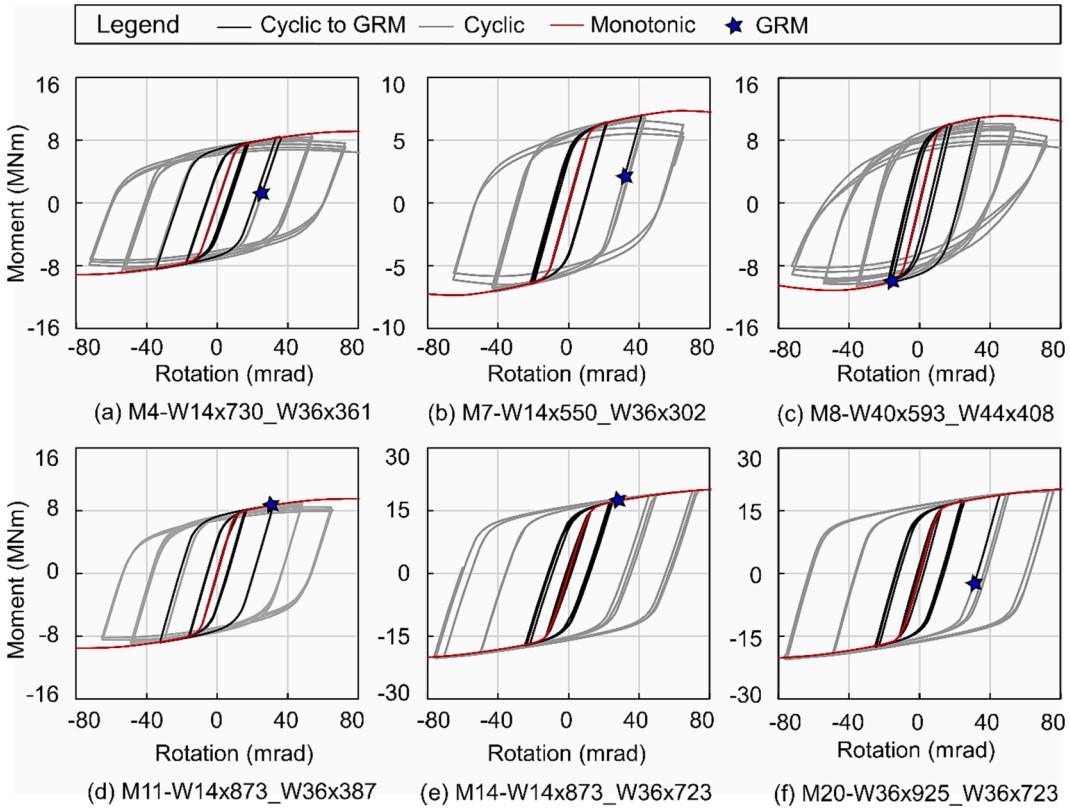


**Fig. 11.** Moment - rotation (M-θ) curves for selected models (labels for subplots are column size, then beam size; notation: GRM – governing response mode).

M8, as shown by the corresponding grey *M-θ* curves in Fig. 11 and the continuum models shown in Fig. 12. This behavior is similar to that of Specimens SP4 and DC3 as discussed in Section 2.

The *M-θ* curves for M14 and M20 complement the qualitative observations from the von Mises maps. At large chord rotations ($\theta_u > 35$ mrad), it is shown that the connection is in the hardening regime due to limited inelastic strains at the RBS, which imposed large strain demands in the beam at the column face (W) leading to an unsatisfactory behavior. The behavior of M14 is similar to that of Specimens SP1 and SP3 described in Section 2.1. For both test members, local buckling did not occur, and the connection sustained significant hardening due to the stocky flanges. This is also confirmed by the relatively large von Mises stresses at the column flange and panel zone compared to those at the RBS, shown in Fig. 12n,t, as well as Fig. 4a,c, respectively. In contrast, M20 resemble a combination of SP3 and SP4. In addition to excessive strains at the welds, the column of both connections twisted.

As observed from Fig. 11, all models developed a stable inelastic response, largely governed by yielding at the RBS. A relatively symmetric hysteretic response is observed in the unloading positive and negative branches of the *M-θ* curves after yielding up to around $\theta > 35$ mrad (at which fracture may occur as discussed below). Note that the models from the parametric investigations were run up to a

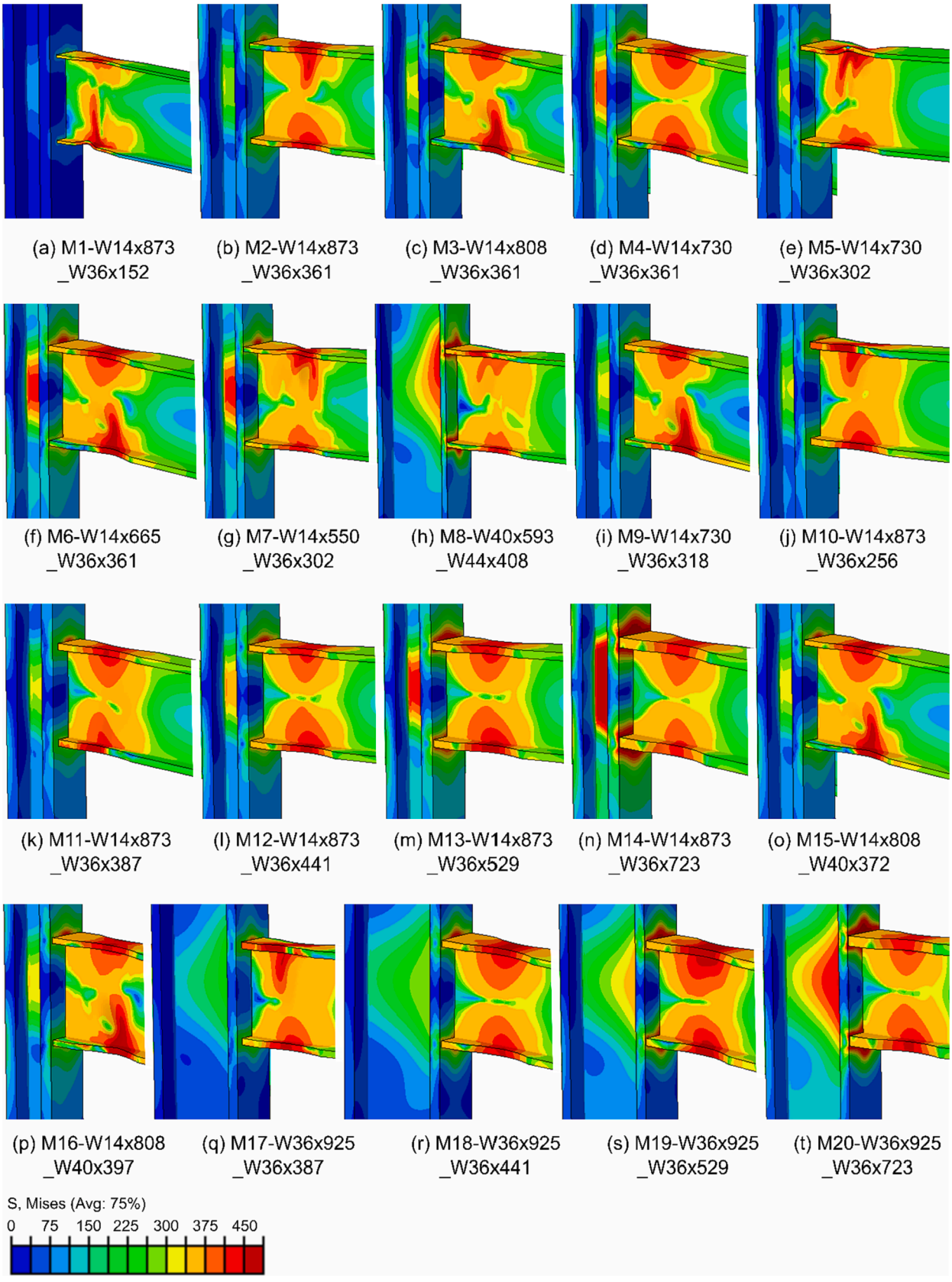


**Fig. 12.** Von Mises stress maps for parametric studies (labels for subplots are column size, then beam size).

displacement corresponding to above 75 mrad, which exceeds the typical seismic demands. Models M14 and M20 would have shown a descending segment beyond 100 mrad, which is significantly higher than most extreme rotations imposed by seismic loading. For such connections, the likelihood of fracture at beam-to-column welds would precede any local buckling. To evaluate the governing response mode (GRM), the analytical criteria described in Section 4 for fracture and local buckling were used. These approaches are widely and consistently used in the literature to verify connection response, as mentioned in Section 4 above.

To obtain a detailed insight into the response of the selected models, contributions of the RBS and column web PZ to the total joint rotation were assessed. These are depicted in the sub-plots of Fig. 13. The rotation at the RBS was assessed from the relative displacements of the top and bottom RBS cuts, normalized by the beam depth. The column web rotation was determined from the resulting relative web displacements and relative vertical panel displacements [76]. As noted in previous studies, the column provides an insignificant contribution to the total energy dissipated by the connection; hence, for the assessments herein, its contribution was disregarded.

In addition to the RBS and PZ contribution, Fig. 13 shows von Mises maps as well as shear stresses $\tau$ at the PZ, and normal stresses σ at RBS. Grey to black curves indicate the increase in stresses with the increase in cycles. The shear stresses $\tau$ were extracted along a path at the mid-height of the PZ, whilst normal stresses σ at RBS were extracted along a path at the center of the reduced section; $\tau_y$ corresponds to the yield shear stress of the steel in the column and $f_y$ is the yield strength of the steel in the beam. As shown in the figure, except for M14, the PZ had an elastic behavior with $\tau < \tau_y$, leading to elastic-only rotations of the component. For M14, the entire PZ achieved $\tau > \tau_y$ and contributed by about 10 % to the total joint rotation. For Model M20 with a deep column, the column web panel reached $\tau_y$ at its interior side due to out-of-plane bending of the connection and column twist, whilst the shear deformations were largely elastic. This is confirmed by the $M$-$\theta_{PZ}$ curve in the panel of Fig. 13f, which does not show any inelastic deformation.

In terms of RBS stresses, Models M4, M6, M7 and M11 show initiation of local flange buckling. This is associated with elastic stresses in the column flange as indicated by green or blue color in the von Mises stress maps. In contrast, the stresses at the RBS of M14 and M20 reached $f_y$ both in tension and compression, but there was no sign of buckling. Moreover, for both connections, the von Mises stresses in the column flanges are above yield indicating high demands increasing fracture susceptibility. It is also worth noting that although M11 seems to have a good response, buckling at the RBS is largely associated with beam web buckling and the beam tension flange has a high concentration of stresses near the beam-column welds. The above points suggest a gradual shift from RBS local buckling response (M4, M6, M7) to potential fracture at the welds and/or column flange (M14, M20).

### 5.2. Plastic strain distributions

As shown in Figs. 14 and 15, the overall inelastic strain distribution of the numerical models varied depending on their component characteristics. The equivalent plastic strains $\xi$, are plotted against the chord rotations $\theta$ in Fig. 14, and against the number of inelastic cycles in Fig. 15, for selected models. As noted in Section 4, for $\xi = 0$, the material is in the elastic regime, whilst $\xi > 0$ signifies yielding. The ξ levels are analyzed at the RBS, W, PZ and CF. Fig. 15 also includes the plastic strain life (PSL), local buckling (LB) criteria and the governing response mode (GRM). As noted above, GRM indicates largest equivalent plastic strain at a connection component intersecting the governing criteria described in Section 4. The criteria were assessed using the same principles described in Section 4, noting that for LB assessments, the aspect ratio of the flange varied between 4.65 and 9.48 for the models described in this

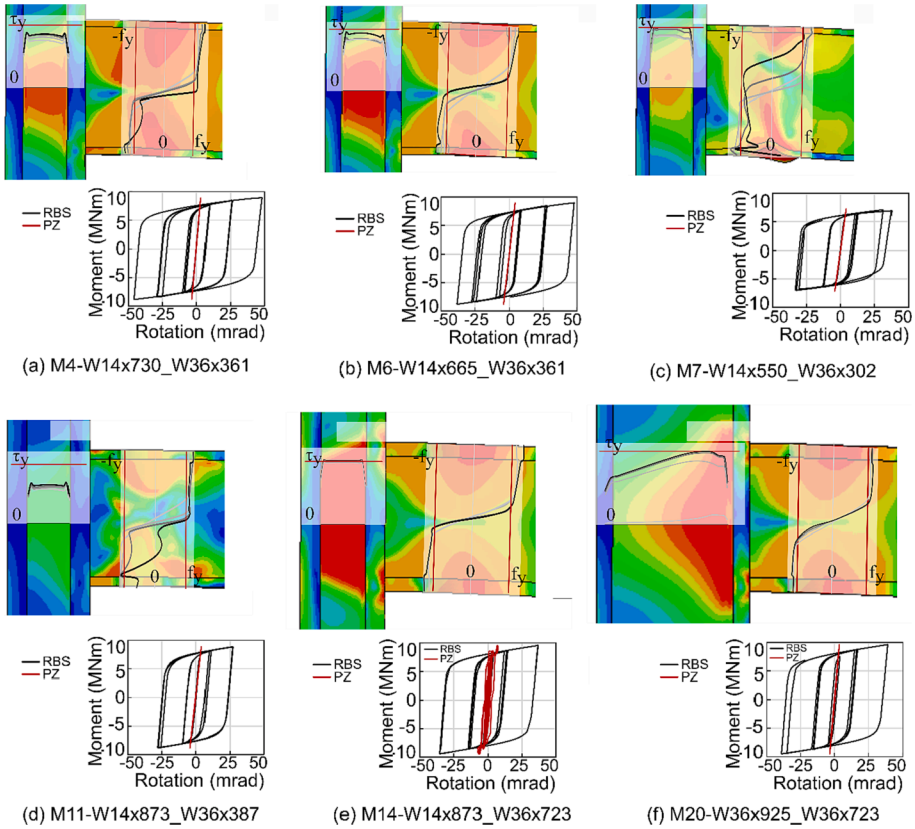


**Fig. 13.** Shear stress (τ) in the column web PZ and normal stress (σ) at the RBS for selected models (Notes: grey to black curves represent increase in stresses with increase in cycles; the plots in the sub-panels represent the rotations of the RBS and PZ; labels for subplots are column size, then beam size).

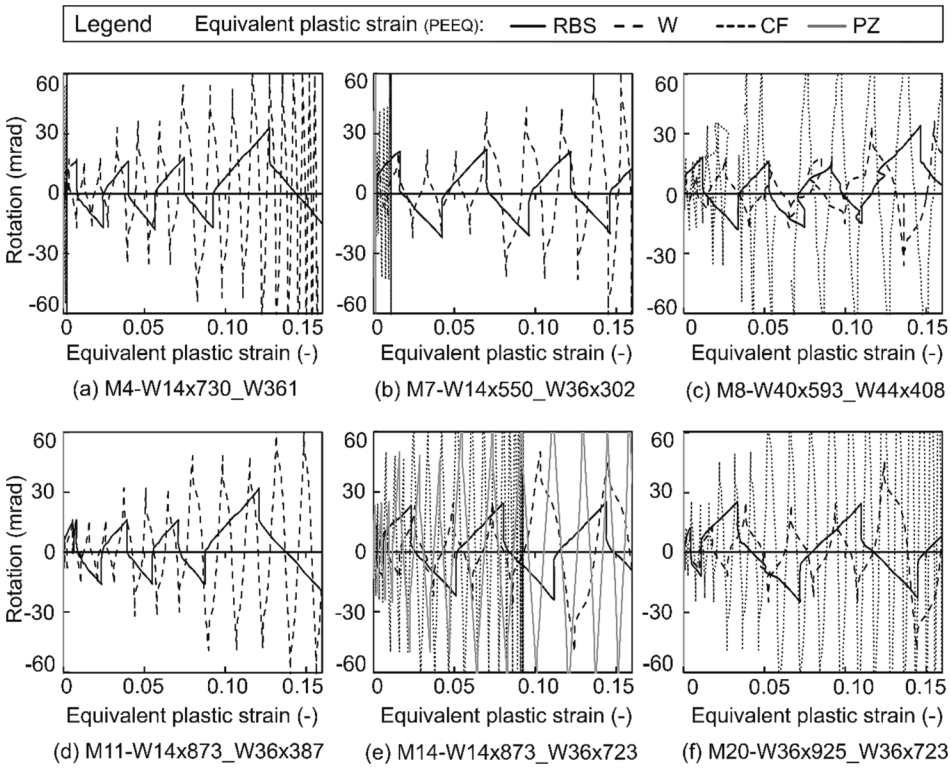


**Fig. 14.** Plastic scalar development (ξ) versus chord rotation (θ) for models (Notations: RBS – reduced beam section, W – welds, CF – column face, PZ – panel zone; labels for subplots are column size, then beam size).

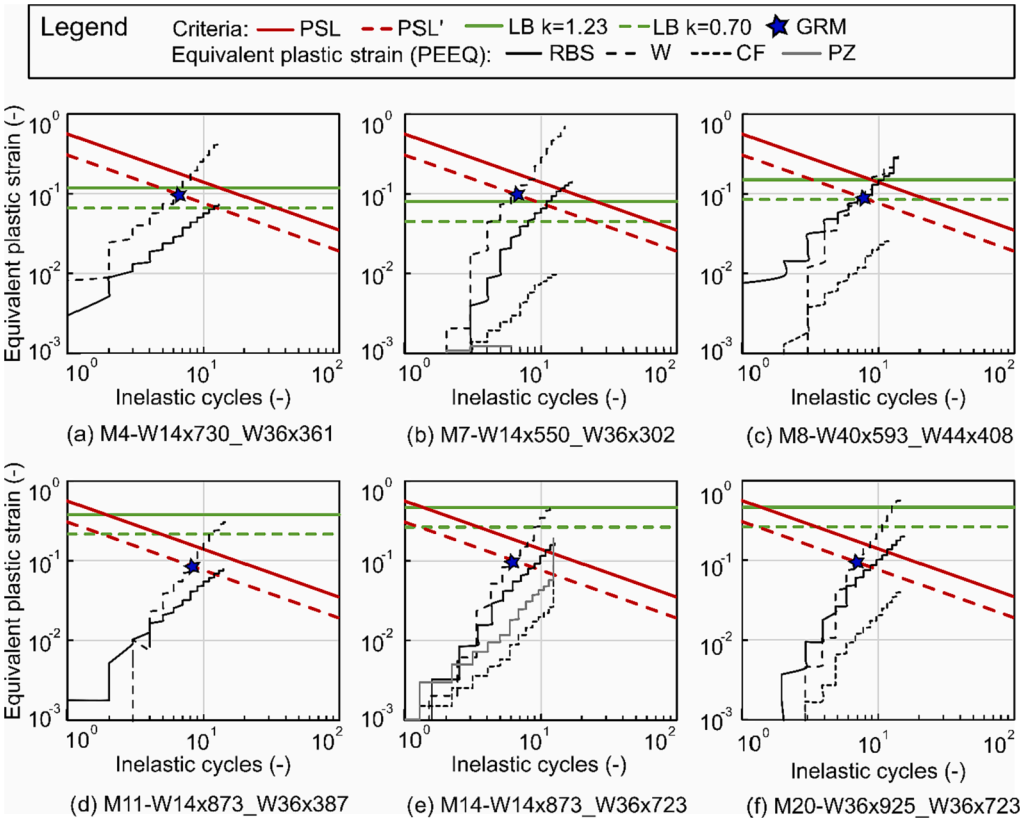


**Fig. 15.** Ultra-low cycle fatigue plot for models (Notations: PSL – plastic strain life using average CM parameters, PSL' – translated PSL using $\lambda_{f,min}$,CM – Coffin Manson, LB – local buckling, GRM – governing response mode, RBS – reduced beam section, W – welds, CF – column face, PZ – panel zone; labels for subplots are column size, then beam size).

section.

As depicted in Fig. 14a,b, for M4 and M7, respectively, the plastic strains at the RBS are consistently higher than at the other components for $\xi \leq 0.15$. This is shown by a narrower $\theta$ range for RBS, compared to W, PZ and CF at the same $\xi$. Based on the plots in Fig. 15a,b, any limit condition would appear at W. As buckling is unlikely to occur at the W due to the inherent stiffening of the beam flange by the column, the next condition would be LB at RBS. As $\xi$ are plotted at a single point in the continuum, consistently at the same location in all models for comparative purposes (flange mid-depth at centre of the RBS, and at the beam top flange for W at the column face), LB may govern at RBS for M4 and M7 if the equivalent plastic strains would be plotted at the point of maximum strains and would precede fracture at the locations investigated. For M11, although the $\xi$ shown in Fig. 14d for $\xi \leq 0.15$ are greater at RBS than the other components, this is associated with beam web buckling. This is also shown in Fig. 15d that suggests that local buckling (LB) at the RBS is not governing.

On the other hand, for M8, M14 and M20, the inelastic strains at the RBS are of similar magnitude to those at W ($\xi$ at CF and PZ are lower), suggesting large demands at welds, that can lead to fracture (Fig. 14c,e,f). As noted above, further cycling beyond GRM would have produced post-peak degradation in M8 due to out-of-plane connection rotation. Moreover, Fig. 15c shows that the inelastic strain curves for W and RBS intersect the plastic strain life (PSL) curve nearly at the same point, before local buckling (LB) would occur. For M14 and M20, both the $\xi$-$\theta$ curves in Fig. 14e,f and low-cycle fatigue plots in Fig. 15e,f, respectively, indicate that LB is highly unlikely and fracture at W is governing. As noted for the stress distributions at RBS and PZ from Fig. 13, the plastic strain development indicates a gradual shift from RBS buckling response (M4, M7) to potential fracture at the welds or column flange (M8, M14, M20). This gradual transition is proportional to the increase in beam weight (Fig. 2a), with connections closer to the code limit having a buckling-governed response, whilst connections towards the right-end of the numerical dataset being more susceptible to fracture.

As pointed out in Section 2, SP1 and SP3, which are also at the right-end of the numerical dataset in Fig. 2a, had a relatively brittle behavior, which was attributed to the extreme demands on the relatively thick welds. Although the welds were not explicitly modelled, the plastic strain development at the main connection components indicate the same response. For SP1, the $\xi$ levels shown in Fig. 16 are similar at W and RBS until nearly the last cycles, whilst they are lower at the PZ. In SP3, $\xi$ is higher at W than at RBS. This response is also indicated in the ultra-low cycle fatigue plots from Fig. 10a,c for SP1 and SP3, respectively. As the relationship between $\xi$ and $\theta$ for various connection components can be used as a reference to characterize the connection behavior, a complementary sensitivity study was carried out in which the geometry and location of the reduced section of SP1 and SP3 were varied. This was primarily undertaken to investigate alternative designs in which the plastic strains at the welds (W) are minimized and a higher plastic concentration is promoted at the reduced section (RBS). According to North American design procedures (ANSI/AISC 358–16), the limits on the RBS geometry are a function of the beam width ($b_f$) and depth (d) as follows: the distance from the column face varies within $0.5 \times b_f \leq a \leq 0.75 \times b_f$, the length of the RBS is in the range $0.65 \times d \leq b \leq 0.85 \times d$, and the depth of cut at the middle of the RBS is $0.1 \times b_f \leq c \leq 0.25 \times b_f$. These ranges are similar in Eurocode 8–3 [18]: $a = 0.5 \times b_f$, $b = 0.75 \times d$ and $c = 0.20 \times b_f$.

A total of five models were constructed for each of the two configurations (SP1 and SP3). In these models, the key geometrical characteristics, listed in Table 4, were varied within the prescribed code limits as well as to beyond code ranges up to $a = 0.33 \times b_f$ and $c = 0.33 \times b_f$. The depth of cut was limited to $0.33 \times b_f$, as beyond this limit the flange width at the RBS would be below 35 % of the corresponding non-RBS section, reducing significantly the moment capacity and increasing susceptibility to local instabilities.

The development of $\xi$ for SP1 models in Fig. 16 indicates that a

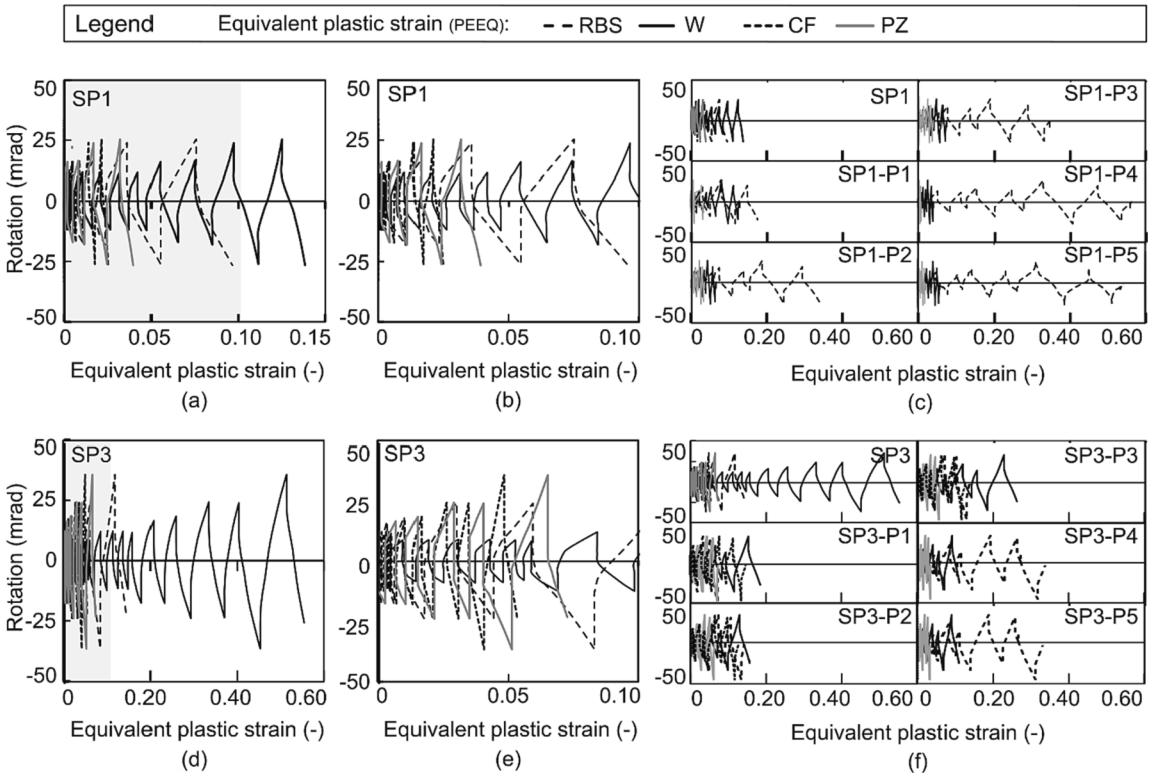


**Fig. 16.** Plastic strain scalar development with increase in cycles up to failure for: a) SP1 to ultimate, b) SP1 to $\xi \approx 0.15$, c) SP1 models with modified RBS geometry, d) SP3 to ultimate, e) SP3 to $\xi \approx 0.15$, f) SP3 models with modified RBS geometry (Notations: W – welds, RBS – reduced beam section, PZ – panel zone, CF – column face; labels for subplots are column size, then beam size).

reduction in the distance between the RBS root and column face would have an insignificant influence in terms of limiting the strains at the weld in comparison to a deeper trimming of the flanges (e.g. SP1-*P2* vs SP1-*P3*). For example, the development of $\xi$ in SP1-*P2* vs SP1-*P3* ($a/b_f =$ 0.50 and $c/b_f = 0.25$ vs $a/b_f = 0.33$ and $c/b_f = 0.25$, respectively) or SP3-*P4* vs SP3-*P5* ($a/b_f = 0.33$ and $c/b_f = 0.33$ vs $a/b_f = 0.5$ and $c/b_f = 0.33$, respectively) have similar values. SP1-*P1* ($a/b_f = 0.50$ and $c/b_f = 0.18$) and SP3-*P2* ($a/b_f = 0.50$ and $c/b_f = 0.25$) had RBS strains that were slightly higher than at W, suggesting that an RBS cut in the range of $c = 0.25 \times b_f$ would facilitate a good hysteretic response. However, for improved safety, a cut depth at the middle of the RBS of $c = 0.33 \times b_f$ should be considered. SP1-*P4*, SP1-*P5*, SP3-*P4* and SP3-*P5* show a behavior governed primarily by the RBS, with strains at the reduced section substantially larger compared with other models. It is worth noting that such an increase in the cut depth at the RBS is associated with a reduction in moment capacity of up to 30 % in comparison to the test configuration.

### 5.3. Comparative evaluations and recommendations

An increase in the depth of the RBS cut is associated with an overall reduction in plastic moment capacity, with a reduction in flange slenderness whilst web slenderness remains the same. For jumbo beam sections, a more compact RBS flange (small $b_{RBS}/2t_f$ values) would limit the development of local buckling, hence web buckling may govern due to limited restraint from flanges. Jumbo beam sections implicitly have stocky flanges without a reduced section; they are classified as 'compact' as per AISC 360–16 [32] if $0.5b_f \times f_y^{0.5}/t_f \leq 257$ (assuming $E = 210$ GPa), and 'Class 1′ to Eurocode 3–1-1 [81] if $0.5b_f \times f_y^{0.5}/t_f \leq 183$ (assuming $b' = 0.75 \times c'$, where $b' = b_f/2$, $b_f$ is the total flange width, $c'$ is the length of the outstand flange, and $b'/c' = 0.75$ is the average ratio for the sections from the database in Table 4). Note that the section classification to the above codes is a function of $b'/t_f$ or $c'/t_f$, $f_y$, amongst other parameters, and the limits shown above were converted as a function of $0.5b_f \times f_y^{0.5}/t_f$ for consistency ($f_y$ is the yield strength and $t_f$ is the flange thickness).

With reference to Fig. 2a, all beam sections with beam weights $w \geq 449$ kg/m evaluated in this paper belong to 'compact' and 'Class 1′ for flange classification. These also comply with the more stringent requirements for flanges of 'highly ductile members' per AISC 341–16 [31] ($0.5b_f \times f_y^{0.5}/t_f \leq 137$, assuming an elastic steel modulus of $E = 210$ GPa and ratio between the measured and specified yield strength of $R_y = 1.15$). Sections with $w < 449$ kg/m tend to be at or below this limit (e.g. SP2 with $0.5b_f \times f_y^{0.5}/t_f = 139$). Webs of beams with $w \geq 449$ kg/m are classified as 'compact' ($h \times f_y^{0.5}/t_w \leq 1723$) and Class 1 ($h \times f_y^{0.5}/t_w \leq 1104$) according to AISC 360–16 [32] and Eurocode 3–1-1 [81], respectively ($h$ is the depth between fillets, and $t_w$ is the web thickness). Some webs of beams with w < 449 kg/m are 'compact' and Class 2 (SP2, DC1, and DC2 with $h \times f_y^{0.5}/t_w = 1300$, 1146, and 1184, respectively). These sections, and those of models M5,7,8 ($w \geq 449$ kg/m) are below the requirements of AISC 341–16 [31] for webs which are 'highly and moderately ductile' ($h \times f_y^{0.5}/t_w \leq 671$).

Although all these sections develop their plastic moment capacity (i.e.'compact' [32] and Class 1 or 2 [81]), they have different rotation capacities, and those with comparatively more slender flanges are likely to develop inelastic buckling at RBS, as discussed in Sections 2 and 5. These cross-sections are associated with $3.40 < 0.5b_f/t_f < 5.00$ or $37.8 < 0.5b_f \times f_y^{0.5}/t_f < 55.4$ and are in RBS connections, designed to current provisions, with $0.12 < \lambda_M = (M_{RBS}/M_{col}) \times (a/d)^{0.33} < 0.32$. The parameter $\lambda_M$ is a proposed moment capacity ratio, in which $M_{RBS}$ is the plastic moment capacity at the RBS, $M_{col}$ is the column moment capacity, $a$ is the distance from the column face to the center of the RBS and $d$ is the depth of the beam. Conversely, beam sections with stockier flanges from the numerical database in Fig. 2a that comply with the 'highly ductile members' classification of AISC 341–16 [31], representative of beams with weights up to threefold the prescribed weight limit, are likely to exhibit significant hardening without inelastic buckling at the RBS. These sections have flange slenderness ratios $2.10 < 0.5b_f/t_f < 3.70$ or $25.4 < 0.5b_f \times f_y^{0.5}/t_f < 41.5$, and are in connections with relatively high RBS-to-column moment capacity ratios ($0.25 < \lambda_M < 0.83$). For RBS connections with such sections, significant hardening may facilitate extreme demands at welds leading to fracture. Although all sections are 'compact' [32] and Class 1 or 2 [81], jumbo sections that do not satisfy the comparatively more stringent seismic section classification requirements [31], are prone to inelastic buckling at the RBS as evidenced by the experimental and numerical results described this paper.

A lower moment capacity at the RBS would reduce the ratio between moment capacities of the RBS and the column ($M_{RBS}/M_{col}$), minimizing the strains in the beam at the column face, and reducing the demand at the welds. This is captured by the results in Table 4 which show that an increase in the RBS cut depth reduced significantly the equivalent plastic strain ratio $\mu_\xi = \xi_W/\xi_{RBS+PZ}$. The parameter $\xi_W$ is the equivalent plastic strains at the welds and $\xi_{RBS+PZ}$ is the sum of the equivalent plastic strains recorded at the RBS and PZ, at 20 mrad joint rotation. This level of rotation corresponds to yielding in the joint but without any sign of local instability.

As indicated in Table 4, considering an RBS cut of $c = 0.33 \times b_f$ (i.e. 66% of the full flange width) reduced the $\mu_\xi$ ratio by 80 % for SP1 (i.e. SP1-*P5*) and by 56 % for SP3 (i.e. SP3-*P3*), compared to the original designs. However, a smaller cut in the range of $c = 0.25 \times b_f$ (i.e. 50% of the full flange width) may be sufficient to mobilize extensive yielding at the RBS, without leading to excessively high inelastic strains at W. Table 4 also indicates more than half of the models achieved relatively high rotations ($\theta_u > 35$ mrad), suggesting that those connections are likely to have a good hysteretic response and may satisfy the qualification per AISC seismic provisions [17]. Note that this assessment is based on the procedure described in Section 4 which includes a number of assumptions for determining the likelihood of weld fracture and local buckling, as well as the governing response mode (GRM). The AISC qualification criterion requires that a beam-column connection completes one cycle at 4 % story drift, corresponding to 40 mrad chord rotation and includes all sources of deformation (beam, panel zone, and column), while retaining 80 % of the nominal plastic moment strength of the unreduced beam section.

Depending on the design of the RBS connection, the three main sources of deformation contribute differently to the overall rotation for qualification, but only the cumulative θ is measured. Whilst the column rotation is around 10 % of the total joint chord rotation θ in the inelastic regime [29], the ratio between the rotations at the PZ and RBS varies depending on the design assumptions and can be correlated with the $M_{RBS}/M_{col}$ ratio. As discussed in Section 2.1, in SP1-4, 53–83 % of θ occurred at the RBS and 0–33 % at the PZ, whilst for DC1-3 up to 25 % of the θ was at the PZ. In the models, up to around 10 % of θ was at the PZ as shown in Fig. 13. These RBS connections were designed with a relatively stronger column in comparison to SP1-4 and DC1-3 (i.e. comparatively smaller $M_{RBS}/M_{col}$). It is worth noting that in ordinary beam-to-column connections with non-jumbo sections, weak PZ designs can result in very high distortional demands at the welds [2]. In RBS connections with non-jumbo sections, yielding is forced at the reduced section and the demand at welds is minimized. However, this is not the case of RBS connections designed to current codes and with jumbo beams of $3.40 < 0.5b_f/t_f < 5.00$ or $37.8 < 0.5b_f \times f_y^{0.5}/t_f < 55.4$ which exhibit significant hardening. For such connections, a relatively high $M_{RBS}/M_{col}$ ratio and an elastic PZ may be needed to facilitate substantial inelasticity at the RBS.

Fig. 17 depicts the relationship between $\mu_\xi$ and a proposed capacity ratio $\lambda_M = (M_{RBS}/M_{col}) \times (a/d)^{0.33}$ for the parametric assessments from this section, in which $M_{RBS}$ is the plastic moment capacity at the RBS, $M_{col}$ is the column moment capacity, $a$ is the distance from the column face to the center of the RBS and $d$ is the depth of the beam. Based on the assessments from Sections 5.1 and 5.2, a good response is correlated with $\mu_\xi < 0.66$ and $\lambda_M \leq 0.45$. This indicates that the RBS cut depth and

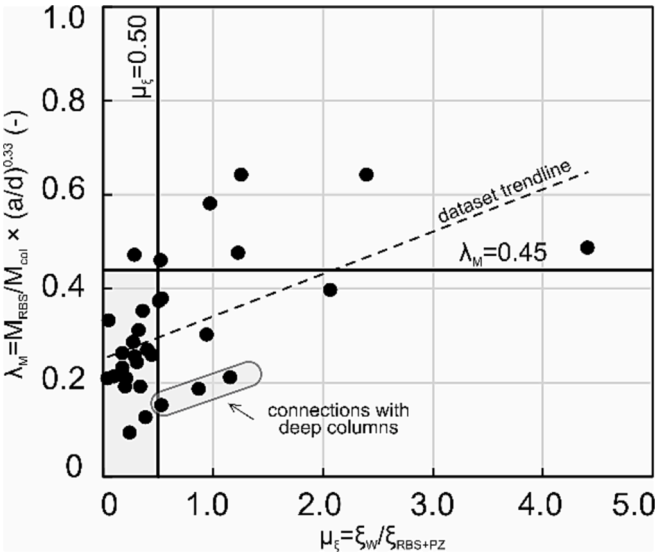


**Fig. 17.** Relationship between the equivalent plastic strain ratio ($\mu_\xi$) and the proposed capacity ratio ($\lambda_M$).

its position relative to the column face needs to be adjusted to obtain $\lambda_M \leq 0.45$. However, this is only valid for relatively compact columns. As shown in Fig. 17, although $\lambda_M \leq 0.45$, for deep columns $\mu_\xi$ can exceed values of 1.0 indicating high strain demands at the welds. This is clearly shown by the von Mises maps for models M8, M19, M20 in Fig. 12. In these cases, the relatively thin column flanges with respect to beam flanges and high column web slenderness produce an unsatisfactory connection response, characterized by excessive deformations in the column components.

The above observations suggest that for RBS connections incorporating large beam sections above W44 × 408, similar to those investigated in this paper, a deeper cut up to $c \approx 0.33 \times b_f$ and $\lambda_M \leq 0.45$ should be considered to concentrate the inelastic deformation at the RBS. It should also be noted that this approach is suitable only for compact columns. Deep columns with non-stiffened panel zones and with depths outside of the code ranges (i.e. ≥ W36) may be used in conjunction with W36 beams sections when $\lambda_M \leq 0.19$. For such sections, the combined stress at the column flange resulting from in-plane and out-of-plane bending stresses, and warping stresses due to torsion, need to be verified [24]. The out-of-plane bending of the connection can be limited by providing supplementary lateral bracing at the RBS, minimizing the column twist. For beams that do not support a slab, a lateral brace should be provided outside the reduced section of the beam and of the area of expected plastic behaviour [77,78]. The location of the supplemental bracing should be evaluated using the existing code provisions for beam lateral support and for beam flange and web slenderness limits [32,79,80].

The above-suggested approach may lead to reduced distortional demands which are known to cause poor behavior of other components of the connection, particularly in the welds [2]. It should also be noted that beam-to-column RBS connections incorporating beam sections below or equal to W44 × 408 (W1100 × 400 × 607), and columns with depths below W36 (W920), can be designed using current seismic procedures as the test observations from Section 2 and those from the nonlinear analysis described in Section 5 indicated a ductile and stable cyclic performance.

## 6. Concluding remarks

The performance of reduced beam section (RBS) beam-to-column connections incorporating large steel profiles was examined through detailed nonlinear numerical assessments, validated against results from two test series. The investigation included a parametric evaluation in which either the column-to-RBS or RBS-to-beam moment capacity ratios were varied. The numerical results, combined with the analytical evaluations and test observations, enabled an in-depth assessment of the failure modes and distribution of plasticity within the connection. Several key remarks are outlined below.

- The experimental and numerical results showed that the stiffness, strength, ductility, hysteretic response and failure modes of such connections are dependent on the beam and column section sizes. Compared to conventional RBS connections, for connections with jumbo sections, a higher concentration of stresses may occur at the column panel zone or the column flanges, with lower stress levels developing at the RBS. From the main sources of the connection deformation, in the inelastic regime, the reduced section mobilizes 53–83 % of the deformation, whilst the panel zone is between 0 and 33 %, and the column is around 10 %. Although all components contribute to the joint deformation, the cumulative rotation is required for qualification procedures.
- The parametric investigations showed that RBS connections from the numerical database with comparatively low RBS-to-column moment capacity ratios ($0.12 < \lambda_M < 0.32$), which incorporate jumbo beam sections with flanges characterized by $37.8 < 0.5b_f \times f_y^{0.5}/t_f < 55.4$, are likely to fail due to extensive yielding followed by local buckling at the RBS, exhibiting limited hardening. These sections are classified as compact, but generally do not satisfy the comparatively more stringent seismic cross-section section classification requirements according to current seismic provisions.
- Conversely, RBS connections from the numerical database with comparatively high RBS-to-column moment capacity ratios ($0.25 < \lambda_M < 0.83$), which incorporate jumbo beam sections with flanges characterized by $25.4 < 0.5b_f \times f_y^{0.5}/t_f < 41.5$, representative of beams with weights up to threefold the prescribed weight limit, are likely to exhibit significant hardening that may facilitate extreme demands at welds leading to fracture. These sections are classified as compact and satisfy the requirements for highly ductile members stipulated in current seismic provisions.
- For relatively deep columns (W36 and W40), the force induced from the beam flanges, combined with RBS flange buckling, could produce out-of-plane column rotation. To avoid column twist and to develop a behavior characterized by a stable hysteretic response and desirable ductility levels, such connections should be provided with bracing outside the reduced section of the beam and of the region of expected plastic behavior.
- The above observations indicate the need for an alternative design procedure for RBS connections incorporating jumbo sections to reduce the excessive strain demands at the beam-to-column welds for beams with very thick flanges. The findings of the numerical study point to the need for a deeper RBS cut in the range of 66 % of the beam width (i.e. $c = 0.33 \times b_f$) while maintaining the same ranges for the length ($0.65 \times d \leq b \leq 0.85 \times d$) and position of the cut with respect the column face ($0.5 \times b_f \leq a \leq 0.75 \times b_f$), as well as maintaining the RBS-to-column moment capacity ratios at appropriate levels. Further experimental verification of the proposed RBS cut is nonetheless needed.
- For connections incorporating relatively deep columns, more stringent design requirements may need to be followed. For such connections, the capacity ratio proposed in this paper should be about half of that for connections with compact columns. In general, the findings of this investigation indicate that RBS connections with jumbo beam and columns can be used in practice provided that the proposed geometry-specific design and detailing rules are followed.

## CRediT authorship contribution statement

**D.V. Bompa:** Conceptualization, Data curation, Formal analysis,

Investigation, Methodology, Visualization, Software, Writing - original draft. **A.Y. Elghazouli:** Conceptualization, Funding acquisition, Resources, Writing – review & editing. **T. Bogdan:** Conceptualization, Writing – review & editing. **M.R. Eatherthon:** Conceptualization, Funding acquisition, Resources, Writing – review & editing. **R.T. Leon:** Conceptualization, Funding acquisition, Resources, Writing - review & editing.

## Declaration of Competing Interest

The authors declare that they have no known competing financial interests or personal relationships that could have appeared to influence the work reported in this paper.

## Data availability

Data will be made available on request.

*Acknowledgements*

The financial support from the Research Fund for Coal and Steel of the European Community through the project EQUALJOINTS (Grant agreement no. RFSR-CT-2013-00021), as well as from Virginia Tech, for the experimental assessments in this paper are gratefully acknowledged. The numerical investigations were also supported by the Research Fund for Coal and Steel of the European Community through the project EQUALJOINTS-PLUS (Grant agreement no 754048-2017).

**Data Availability Statement.** Data will be made available on request.

## References

[1] Elghazouli, A.Y., (2015). Seismic Code Developments for Steel and Composite Structures. In: Ansal A. (eds) Perspectives on European Earthquake Engineering and Seismology. Geotechnical, Geological and Earthquake Engineering, vol 39. Springer, Cham doi: 10.1007/978-3-319-16964-4_5.

[2] Castro JM, Dávila-Arbona FJ, Elghazouli AY. Seismic design approaches for panel zones in steel moment frames. J Earthq Eng 2008;12:34–51. https://doi.org/10.1080/13632460801922712.

[3] SAC. Survey and assessment of damage to buildings affected by the Northridge Earthquake of January 17, 1994, SAC95-06. Sacramento: SAC Joint Venture; 1995.

[4] Popov EP, Yang TS, Chang SP. Design of steel MRF connections before and after 1994 Northridge earthquake. Eng Struct 1998;20(12):1030–8. https://doi.org/10.1016/S0141-0296(97)00200-9.

[5] Plumier, A. (1990). New idea for safe structures in seismic zones, IABSE Symposium: Mixed structures including new materials, Brussels, p. 431-6. doi: 10.5169/seals-46518.

[6] Plumier A. The dogbone: back to the future. Engineering Journal, American Institute of Steel Construction 1997;34:61–7.

[7] Engelhardt MD, Fry G, Jones S, Venti M, Holliday S. Behavior and design of radius cut reduced beam section connections. A Draft Report of SAC Task 2000;7.

[8] Iwankiw N.R., Carter C.J., (1996). Dogbone: a new idea to chew on, Modern Steel Construction, pp. 18-26, April.

[9] Chen S, Yeh C, Chu J. Ductile steel beam-to-column connections for seismic resistance. J Struct Eng 1996;1292–1299. https://doi.org/10.1061/(ASCE)0733-9445(1996)122:11(1292).

[10] Chen S, Tu C. Experimental study of jumbo size reduced beam section connections using high-strength steel. J Struct Eng 2004;130(4):582–7. https://doi.org/10.1061/(ASCE)0733-9445(2004)130:4(582).

[11] Plumier A, Beg D, Sanchez L. Influence of strain rate, Test report. Université de Liège; 2000.

[12] Engelhardt MD, Winneberger T, Zekany AJ, Potyraj TJ. The dogbone connection: Part II. Mod Steel Constr 1996;36(8):46–55.

[13] Lew HS, Main JA, Robert SD, Sadek F, Chiarito VP. Performance of steel moment connections under a column removal scenario. I: Experiments Journal of Structural Engineering (United States) 2013;139(1):98–107. https://doi.org/10.1061/(ASCE)ST.1943-541X.0000618.

[14] Popov E, Blondet M, Stepanov L, Stojadinović B. Full-Scale Beam-to Column Connection Tests. Berkeley, CA: University of California Department of Civil Engineering; 1996.

[15] Pachoumis D, Galoussis E, Kalfas C, Efthimiou I. Cyclic performance of steel moment-resisting connections with reduced beam sections—experimental analysis and finite element model simulation. Eng Struct 2010;32(9):2683–92. https://doi.org/10.1016/j.engstruct.2010.04.038.

[16] Pachoumis DT, Galoussis EG, Kalfas CN, Christitsas AD. Reduced beam section moment connections subjected to cyclic loading: Experimental analysis and FEM simulation. Journal. Eng Struct 2009;31:216–23. https://doi.org/10.1016/j.engstruct.2008.08.007.

[17] AISC (American Institute of Steel Construction) ANSI/AISC 358-16, Prequalified Connections for Special and Intermediate Steel Moment Frames for Seismic Applications, Chicago, IL.

[18] CEN (European Committee for Standardization) (2005). EN 1998-3 Eurocode 8 — Design of structures for earthquake resistance — Part 3: Assessment and retrofitting of buildings, B-1050 Brussels, Belgium.

[19] Lee CH, Jung JH, Kim SY. Cyclic Seismic Performance of RBS Weak-Axis Welded Moment Connections. Journal of Korean Society of Steel Construction 2015;27(6):513–23. https://doi.org/10.7781/kjoss.2015.27.6.513.

[20] Jones SL, Fry GT, Engelhardt MD. Experimental Evaluation of Cyclically Loaded Reduced Beam Section Moment Connections. J Struct Eng 2002;128(4):441–51. https://doi.org/10.1061/(ASCE)0733-9445(2002)128:4(441).

[21] Zhang, X., Ricles, J. M., Lu, L., Fisher, J. W. (2004) Development of Seismic Guidelines for Deep-Column Steel Moment Connections. Lehigh University, Report Number: 3216.

[22] Zhang X, Ricles JM. Experimental evaluation of reduced beam section connections to deep columns. J Struct Eng 2006;132(3):346–57. https://doi.org/10.1061/(ASCE)0733-9445(2006)132:3(346).

[23] Zhang X, Ricles JM. Seismic behavior of reduced beam section moment connections to deep columns. J Struct Eng 2006;132(3):358–67. https://doi.org/10.1061/(ASCE)0733-9445(2006)132:3(358).

[24] Chi B, Uang C. Cyclic response and design recommendations of reduced beam section moment connections with deep columns. J Struct Eng 2002;128(4):464–73. https://doi.org/10.1061/(ASCE)0733-9445(2002)128:4(464).

[25] Uang CM, Fan CC. Cyclic stability criteria for steel moment connections with reduced beam section. J Struct Eng 2001;127(9):1021–7. https://doi.org/10.1061/(ASCE)0733-9445(2001)127:9(1021).

[26] Uang C, Yu Q, Noel S, Gross J. Cyclic testing of steel moment connections rehabilitated with RBS or welded haunch. J Struct Eng 2000;126(1):57–68. https://doi.org/10.1061/(ASCE)0733-9445(2000)126:1(57).

[27] Landolfo R. European seismic prequalification of steel beam-to-column joints: EQUALJOINTS and EQUALJOINTS-Plus projects. J Constr Steel Res 2022;192:107238. https://doi.org/10.1016/j.jcsr.2022.107238.

[28] Landolfo, R., D'Aniello, M., Tartaglia, R., Constanzo, S., Demonceau, J.F., Jaspart, J.P., Stratan, A., Jakab, D., Dubina, D., Elghazouli, A. and Bompa, D. (2018). EQUALJOINTS PLUS-Volume with pre-normative design recommendations for seismically qualified steel joints. ECCS. Available at: https://www.steelconstruct.com/eu-projects/equaljoints/documents/ [accessed 15 July 2019].

[29] Paquette J, Pepin G, Eatherton MR, Leon R, Nunez E, Webber L, et al. Experimental Investigation of Reduced Beam Section Moment Connections for Steel Wide Flange Sections, Virginia Tech Structural Engineering and Materials Report 2021;No. CE/VPI-ST-19/02.

[30] Gilton, C., Chi, B. and Uang, C.M., (2000). Cyclic response of RBS moment connections: weak-axis configuration and deep column effects. Rep. No. SAC/BD-00, 23. SAC Joint Venture, San Diego.

[31] AISC (American Institute of Steel Construction) ANSI/AISC 341-16, Seismic Provisions for Structural Steel Buildings, 2016, Chicago, IL.

[32] AISC (American Institute of Steel Construction) ANSI/AISC 360-16, Specification for Structural Steel Buildings, Chicago, IL.

[33] Qi, L., Paquette, J., Eatherthon, M., Leon, R., Bogdan, T., Popa, N., Nunez Moreno, E., (2018). Analysis of Fracture Behaviour of Large Steel Beam Column Connections, 12th International Conference on Advances in Steel-Concrete Composite Structures (ASCCS), doi:10.4995/ASCCS2018.2018.7122.

[34] ASTM (American Society for Testing and Materials) A992/A992M-20 Standard Specification for Structural Steel Shapes. ASTM International, West Conshohocken, PA, United States.

[35] ASTM (American Society for Testing and Materials) A913/A913M-19 Standard Specification for High-Strength Low-Alloy Steel Shapes of Structural Quality, Produced by Quenching and Self-Tempering Process (QST). ASTM International, West Conshohocken, PA, United States.

[36] ASTM (American Society for Testing and Materials) A572/A572M-21e1 Standard Specification for High-Strength Low-Alloy Columbium-Vanadium Structural Steel. ASTM International, West Conshohocken, PA, United States.

[37] ASTM (American Society for Testing and Materials) A370-21 Standard Test Methods and Definitions for Mechanical Testing of Steel Products. ASTM International, West Conshohocken, PA, United States.

[38] AISC (American Institute of Steel Construction) (1997). Seismic provisions for structural steel buildings, 2nd Ed., Chicago, with Supplement No. 1.

[39] Englehardt, M. D. (1998). Design of reduced beam section moment connections. Proc. North American Steel Construction Conference, AISC, Chicago, 1–3 to 1–29.

[40] Clark, P., Frank, K., Krawinkler, H., and Shaw, R., (1997). Protocol for fabrication, inspection, testing, and documentation of beam-column connection tests and other experimental specimens. Rep. No. SAC/ BD-97/02, SAC Joint Venture, Sacramento, California.

[41] DSS (Dassault Systèmes Simulia Corp). ABAQUS, CAE,. Analysis user's manual. Johnston, RI, USA: DSS; 2018. p. 2017.

[42] Bompa, D.V., Elghazouli, A.Y. (2017). Numerical modelling and parametric assessment of hybrid flat slabs with steel shear heads, Engineering Structures, 142, 67-83, 2017. doi:10.1016/j.engstruct.2017.03.070.

[43] Phillips AR, Eatherton MR. Computational study of elastic and inelastic ring shaped–steel plate shear wall behavior. Eng Struct 2018;177:655–67. https://doi.org/10.1016/j.engstruct.2018.10.008.

[44] Swanson JA, Kokan DS, Leon RT. Advanced finite element modeling of bolted T-stub connection components. J Constr Steel Res 2002;58(5–8):1015–31. https://doi.org/10.1016/S0143-974X(01)00098-0.
[45] ECCS (European Convention for Constructional Steelwork) 1986. Recommended testing procedure for assessing the behaviour of structural steel elements under cyclic loads. ECCS.
[46] Bogdan, T., Bompa, D.V., Elghazouli, A.Y., Nunez, E., Eatherthon, M., Leon, R. (2019). Experimental and numerical simulations on RBS connections incorporating large sections, COMPDYN 2019 7th ECCOMAS Thematic Conference on Computational Methods in Structural Dynamics and Earthquake Engineering M. Papadrakakis, M. Fragiadakis (eds.). doi: 10.7712/120119.7346.19822.
[47] Ballio G, Castiglioni CA. A unified approach for the design of steel structures under low and/or high cycle fatigue. J Constr Steel Res 1995;34(1):75–101. https://doi.org/10.1016/0143-974X(95)97297-B.
[48] Nip KH, Gardner L, Davies CM, Elghazouli AY. Extremely low cycle fatigue tests on structural carbon steel and stainless steel. J Constr Steel Res 2010;66(1):96–110. https://doi.org/10.1016/j.jcsr.2009.08.004.
[49] Coffin Jr LF. A study of the effects of cyclic thermal stresses on a ductile metal. Transactions of the American Society of Mechanical Engineers, New York 1954;76:931–50.
[50] Manson, S.S., (1953). Behavior of materials under conditions of thermal stress (Vol. 2933). National Advisory Committee for Aeronautics.
[51] Rice JR, Tracey DM. On the ductile enlargement of voids in triaxial stress fields. J Mech Phys Solids 1969;17(3):201–17. https://doi.org/10.1016/0022-5096(69)90033-7.
[52] Kanvinde A. Predicting fracture in civil engineering steel structures: State of the art. J Struct Eng 2017;143(3):03116001. https://doi.org/10.1061/(ASCE)ST.1943-541X.0001704.
[53] Kanvinde, A.M. and Deierlein, G.G., 2004, August. Prediction of ductile fracture in steel moment connections during earthquakes using micromechanical fracture models. In 13th World conference on earthquake engineering (pp. 1-6).
[54] Li S, Xie X, Cheng C, Tian Q. A modified Coffin-Manson model for ultra-low cycle fatigue fracture of structural steels considering the effect of stress triaxiality. Eng Fract Mech 2020;237:107223. https://doi.org/10.1016/j.engfracmech.2020.107223.
[55] Iyama J, Ricles JM. Prediction of fatigue life of welded beam-to-column connections under earthquake loading. J Struct Eng 2009;135(12):1472–80. https://doi.org/10.1061/(ASCE)0733-9445(2009)135:12(1472).
[56] Khalil Z, Elghazouli AY, Martínez-Pañeda E. A generalised phase field model for fatigue crack growth in elastic–plastic solids with an efficient monolithic solver. Comput Methods Appl Mech Eng 2022;388:114286. https://doi.org/10.1016/j.cma.2021.114286.
[57] Koutromanos I, Tola-Tola A, Eatherton MR. Phase-Field Description of Ductile Fracture in Structural Steel under Cyclic Loading. J Struct Eng 2022;148(7):04022073. https://doi.org/10.1061/(ASCE)ST.1943-541X.0003333.
[58] Kanvinde AM, Deierlein GG. Cyclic void growth model to assess ductile fracture initiation in structural steels due to ultra low cycle fatigue. J Eng Mech 2007;133(6):701–12. https://doi.org/10.1061/(ASCE)0733-9399(2007)133:6(701).
[59] Saykin VV, Nguyen TH, Hajjar JF, Deniz D, Song J. The effect of triaxiality on finite element deletion strategies for simulating collapse of full-scale steel structures. Eng Struct 2020;210:110364. https://doi.org/10.1016/j.engstruct.2020.110364.
[60] Danas K, Castañeda PP. Influence of the Lode parameter and the stress triaxiality on the failure of elasto-plastic porous materials. Int J Solids Struct 2012;49(11–12):1325–42. https://doi.org/10.1016/j.ijsolstr.2012.02.006.
[61] Kiran R, Khandelwal K. A triaxiality and Lode parameter dependent ductile fracture criterion. Eng Fract Mech 2014;128:121–38. https://doi.org/10.1016/j.engfracmech.2014.07.010.
[62] Bao Y, Wierzbicki T. On fracture locus in the equivalent strain and stress triaxiality space. Int J Mech Sci 2004;46(1):81–98. https://doi.org/10.1016/j.ijmecsci.2004.02.006.
[63] Barsoum I, Faleskog J. Rupture mechanisms in combined tension and shear—Micromechanics. Int J Solids Struct 2007;44(17):5481–98. https://doi.org/10.1016/j.ijsolstr.2007.01.010.
[64] Baptista C, Reis A, Nussbaumer A. Probabilistic SN curves for constant and variable amplitude. Int J Fatigue 2017;101:312–27. https://doi.org/10.1016/j.ijfatigue.2017.01.022.
[65] de Jesus AM, Matos R, Fontoura BF, Rebelo C, da Silva LS, Veljkovic M. A comparison of the fatigue behavior between S355 and S690 steel grades. J Constr Steel Res 2012;79:140–50. https://doi.org/10.1016/j.jcsr.2012.07.021.
[66] Dusicka P, Itani AM, Buckle IG. Cyclic response of plate steels under large inelastic strains. J Constr Steel Res 2007;63(2):156–64. https://doi.org/10.1016/j.jcsr.2006.03.006.
[67] Guo Y, Fang C, Zheng Y. Post-fire hysteretic and low-cycle fatigue behaviors of Q345 carbon steel. J Constr Steel Res 2021;187:106991. https://doi.org/10.1016/j.jcsr.2021.106991.
[68] ASTM (American Society for Testing and Materials) E606/E606M-21 Standard Test Method for Strain-Controlled Fatigue Testing. ASTM International, West Conshohocken, PA, United States.
[69] Prinz GS, Richards PW. Demands on reduced beam section connections with out-of-plane skew. J Struct Eng 2016;142(1):04015095. https://doi.org/10.1061/(ASCE)ST.1943-541X.0001360.
[70] Elghazouli AY, Treadway J. Inelastic behaviour of composite members under combined bending and axial loading. J Constr Steel Res 2008;64(9):1008–19. https://doi.org/10.1016/j.jcsr.2007.12.016.
[71] Ballio G, Castiglioni CA. Seismic behaviour of steel sections. J Constr Steel Res 1994;29(1–3):21–54. https://doi.org/10.1016/0143-974X(94)90055-8.
[72] Calado L, Azevedo J. A model for predicting the failure of structural steel elements. J Constr Steel Res 1989;14(1):41–64. https://doi.org/10.1016/0143-974X(89)90069-2.
[73] Salmon CG, Johnson JE. Steel Structures. Design and Behaviour: Harper and Row Publishers, Second Edition; 1980.
[74] CEN. (European Committee for Standardization) EN 1993-1-5 Eurocode 3: design of steel structures - part 1–5: plated structural elements. Brussels 2006.
[75] Gardner L, Fieber A, Macorini L. Formulae for calculating elastic local buckling stresses of full structural cross-sections. Structures 2019;17:2–20. https://doi.org/10.1016/j.istruc.2019.01.012.
[76] Augusto H, da Silva LS, Rebelo C, Castro JM. Characterization of web panel components in double-extended bolted end-plate steel joints. J Constr Steel Res 2016;116:271–93. https://doi.org/10.1016/j.jcsr.2015.08.022.
[77] FEMA-267a.,. Interim guideline: Advisory. supplement to FEMA-267 Federal Emergency Management Agency (FEMA) 1997;no. 1.
[78] Moore KS, Malley JO, Engelhardt MD. Design of reduced beam section (RBS) moment frame connections. Los Angeles: Steel Committee of California; 1999.
[79] FEMA-355d. State of the art report on connection performance Report No FEMA-355D. Federal Emergency Management Agency (FEMA). Washington, D.C.: United States; 2000.
[80] AISC. Seismic Provisions for Structural Steel Buildings, American Institute of Steel Construction (AISC). Chicago: Illinois; 1997.
[81] CEN. (European Committee for Standardization) EN 1993-1-1 Eurocode 3: design of steel structures - part 1–1: plated structural elements. Brussels 2005.